# Detection of Magma Reservoir beneath the Changbaishan Volcanic Region through Seismic Ray Tracing

**Final Technical Report under**
**DOS Contract No. 19AQMM20P0737 (BAA2020-001)**
**(May 1, 2020, to November 30, 2022)**

**December 31, 2022**

**Prepared By**
**Dr. Youlin Chen**
**Array Information Technology**
**(**Now ***EMR Solutions & Technology*****)**
**Advanced Technology Division**
**5130 Commercial Dr. Suite B**
**Melbourne, FL 32940**

**Submitted to**
**United States Department of State**
**Bureau of Arms Control, Verification, and Compliance**
**(*Now* Bureau of Arms Control, Deterrence, and Stability)**
**2201 C Street, NW, RM 3531**
**Washington, DC 20520**

**Approved for Public Release; Distribution Unlimited**

# REPORT DOCUMENTATION PAGE

*Form Approved*
*OMB No. 0704-0188*



| **1. REPORT DATE** *(DD-MM-YYYY)* | **2. REPORT TYPE** | **3. DATES COVERED** *(From - To)* |
|---|---|---|
| 31-12-2022 | Final | 1/5/2020 – 30/11/2022 |

**4. TITLE AND SUBTITLE**

Detection of Magma Reservoir beneath the Changbaishan Volcanic Region through Seismic Ray Tracing

**5a. CONTRACT NUMBER**
19AQMM20P0737

**5b. GRANT NUMBER**

**5c. PROGRAM ELEMENT NUMBER**

**6. AUTHOR(S)**

Youlin Chen

**5d. PROJECT NUMBER**

**5e. TASK NUMBER**

**5f. WORK UNIT NUMBER**

**7. PERFORMING ORGANIZATION NAME(S) AND ADDRESS(ES)**

Array Information Technology, Inc.
7074 Greenway Center Drive, Suite 600
Greenbelt, MD 20770-3574

**8. PERFORMING ORGANIZATION REPORT NUMBER**

**9. SPONSORING / MONITORING AGENCY NAME(S) AND ADDRESS(ES)**

United States Department of State
Bureau of Arms Control, Deterrence, and Stability
2201 C Street, NW
Washington, DC 20520

**10. SPONSOR/MONITOR'S ACRONYM(S)**

US DOS/ADS
(formerly US DOS/AVC)

**11. SPONSOR/MONITOR'S REPORT NUMBER(S)**
ADS-VTN-23G03

**12. DISTRIBUTION / AVAILABILITY STATEMENT**
Distribution Statement A (DoDI5230.24): Approved for Public Release; Distribution Unlimited

**13. SUPPLEMENTARY NOTES**

**14. ABSTRACT**

The unrest of the Changbaishan (CBS) volcano implies a magma reservoir underneath this volcano. To detect and study this magma reservoir, we judiciously selected 97 deep earthquakes near CBS with available seismograms recorded by permanent and temporal stations in NE China. We observed significant S-wave shadows (attenuation) and P-wave delays from many seismograms. Seismic ray tracing simulations show that those rays that exhibit S-wave shadows traverse the topmost upper mantle and the crust, indicating the presence of molten magma at these depths. The P-wave delays are observed over a broader region and commonly traverse the lower part of the upper mantle. It suggests a broad low-velocity zone beneath CBS. Further 3D ray tracing simulations will help determine the location, range, and degree of melting of the magma reservoir.

**15. SUBJECT TERMS**
Volcano, P-wave delay, S-wave shadow, Complete ray tracing

| **16. SECURITY CLASSIFICATION OF:** UNCLASSIFIED | | | **17. LIMITATION OF ABSTRACT** | **18. NUMBER** | **19a. NAME OF RESPONSIBLE PERSON** Rongsong Jih |
|---|---|---|---|---|---|
| **a. REPORT** UNCLASSIFIED | **b. ABSTRACT** UNCLASSIFIED | **c. THIS PAGE** UNCLASSIFIED | SAR | 40+v | **19b. TELEPHONE NUMBER** *(include area code)* 1-202-647-8126 |

**Standard Form 298 (Rev. 8-98)**
**Prescribed by ANSI Std. Z39.18**

# EXECUTIVE SUMMARY

Active intraplate Changbaishan (CBS) volcanoes likely originated from the upwelling of hot and wet asthenospheric materials above the stagnant Pacific slab in the mantle transition zone. The unrest of CBS volcano in the period of 2002 – 2005 means that there may be a magma reservoir/chamber beneath the volcano. Many previous studies have shown low-velocity anomalies in the lower crust or upper mantle and even partial melting of the lower crust beneath the CBS volcano. However, those studies did not provide direct evidence of the existence of a magma reservoir due to the insufficient model resolution limited by the used data and techniques. We detected and studied the CBS magma reservoir from S-wave shadows (attenuation) and P-wave delays in this study. The method exploited the rich seismic records of deep-focus earthquakes near the CBS recorded by densely distributed seismic stations in NE China. These earthquakes occurred within the Wadati-Benioff seismic zone of the subducting Pacific slab. As seismic rays leave the deep-focus source and arrive at surface stations, they can thoroughly scan the crustal and upper mantle area underneath the CBS volcanic region. If low-velocity anomalies are present, P-wave delays are expected to be observed. S-wave shadows are expected if seismic rays pass through a molten medium. We performed complete ray tracing simulations to determine ray patterns and their sensitivities to the variations in velocity structure. We found that the spatial distribution of seismic rays with P-wave delays roughly coincided with low-velocity zones in the upper mantle and crust revealed by seismic tomography for NE China and the CBS Mountains. The spatial distribution of seismic rays with S-wave shadows indicated that the molten magma was limited to small-sized areas of stations showing S-wave shadows. Further ray tracing simulations using more complex models will determine the position, size, and degree of melt of the CBS magma reservoir, which could explain the observed P-wave delays and S-wave shallows, and ultimately help to establish a detailed crustal and upper mantle structure beneath the CBS volcanic region and reconcile the debates on the origin and Earth structure of volcanoes in Northeast Asia.

The main tasks accomplished in the technical progress include:

1. *Seismic Data Collection*: We judiciously selected 97 deep-focus earthquakes along the Wadati-Benioff seismic zone of the subducting Pacific slab. Of these earthquakes, 73 have a magnitude larger than M4.5. These earthquakes were recorded by five temporal seismic networks (1U, XI, XL, YP, and V0) and three permanent networks (HL, JL, and LN) deployed in NE China. Networks 1U, XI, XL, and YP belong to PASSCAL seismic deployments, and we download the waveform data from the IRIS-DMC. Permanent networks HL, JL, and LN are part of the Chinse National Digital Seismic Network (CNDSN), and the temporal network V0 belongs to the Chinarray. The waveform data of the four Chinese networks were retrieved from the Chinese Earthquake Network Center (CENC) and the Institute of Geophysics, CEA, respectively, through the collaboration program between ARRAY and Chinese collaborators.
2. *Data Processing*: Besides the routine data processing for seismograms, such as baseline removal, filtering, and data quality control, we manually picked P- and S-wave arrivals whenever applicable. These observed arrivals were compared to the theoretical predictions from ray tracing calculations. During the data processing, we found the S-waves in some seismograms missing or too weak to be identified.

3. *S-wave Shadows and P-wave Delays*: We quantified S-wave shadow by calculating the ratio of S-wave and P-wave amplitudes and determined P-wave delay by comparing the observed P-wave arrival time with theoretical arrival time.
4. *Complete Ray Tracing*: We employed the Complete Ray Tracing (CRT) method [Červeny et al., 1988] to perform ray tracing simulations. The CRT program controls the ray tracing computation by using input parameters and constructing various 1D and 3D models. Taking advantage of the high flexibility of CRT, we first built a layered model based on the 1D global AK135 model, but the free surface and Moho were replaced by 3D topography. Many stations surrounding the CBS volcanic region show significant S-wave shadows and P-wave delays. S-wave shadows mean the presence of molten magma in the upper mantle or crust, and P-wave delays indicate a low-velocity anomaly beneath the CBS volcano. However, the spatial distribution patterns of S-wave shadows and P-wave delays are inconsistent. The seismic rays with P-wave delays are spread over a larger region than those with S-wave shadows. These observations and results from previous structural models provide us with the knowledge to perform ray tracing simulations using more complex 3D models.

# TABLE OF CONTENTS

# 1 INTRODUCTION

## 1.1 Background

The major volcanic groups in Northeast (NE) Asia are mainly distributed in NE China, some of which are still active today, and some have been considered extinct for a long time. These volcanos are roughly surrounding the Songliao basin (Figure 1). The active volcanos in the north include Arshan, Keluo, and Wudalianchi. The Wudalianchi volcano is one of the youngest volcanic fields in mainland Asia. It is located at the junction between Lesser Khingan (XiaoXing'an) Mountains and the Song-Nen depression, with an area of about 500 km$^2$. The last recorded eruption of this volcano occurred in 1719-1721, and it erupted about 1 km$^3$ of mostly pahoehoe lava.

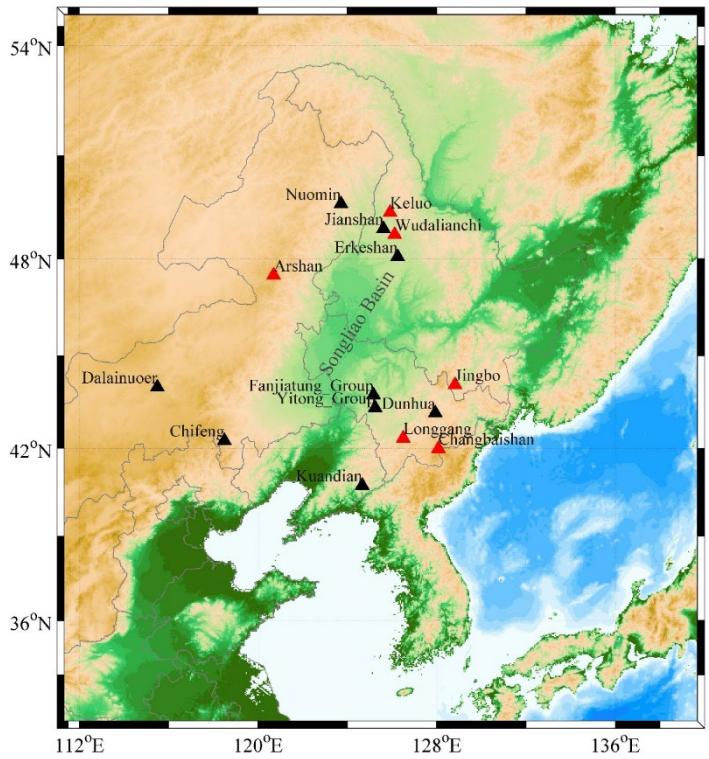


**Figure 1**. Distribution of active (red triangles) and dead (black triangles) volcanos in NE China.

The active volcanos in the south are Jingbo, Longgang, and Changbaishan. The Changbaishan (CBS or Mt. Paektu called in Korea) volcano is the largest volcano in NE Asia, straddling the border between Jilin province, China, and the Democratic People's Republic of Korea (DPRK). CBS volcano has been reported to have erupted many times in history, the largest of which occurred around 969±20, and some small eruptions have occurred in historic times since the 15th century, with the last one occurring in April 1903 [Kang et al., 2011]. An episode of unrest occurred from 2002 to 2005, characterized by significantly increased seismicity with shallow focal depth (< 5km), ground deformation with Mogi source at 2 to 6km measured by GPS, fluid geochemical anomalies, and emission of volcanic gases [e.g., Xu et al., 2012; Wei et al., 2013]. It showed that the CBS volcano continues to be active, but the origin, evolution history, and internal structure of this volcano remain to be debated in detail. Longgang and Jingbo are two smaller volcanos located west and north of the CBS volcano, respectively. Longgang volcano is ~136km from CBS volcano and reportedly erupted around 350AD. Jingbo volcano, ~241km from CBS, is

a young volcanic field in NE China. It is unknown whether the unrest of the CBS volcano is related to these two smaller volcanos until the underlying structure of this area is carefully investigated.

Since the CBS volcano lies far from any tectonic plate boundary, it is difficult to explain this intraplate volcano using the plate tectonic paradigm. Some researchers proposed that the origin of this intraplate volcano was associated with the upwelling of hot and wet asthenospheric materials in the big mantle wedge above the stagnant part of the Pacific slab lying horizontally in the mantle transition zone (410-660km depth) beneath the Korean Peninsula [e.g., Zhao and Tian, 2013] (Figure 2a). In this "big mantle wedge" model, dehydration occurred in the transition zone and resulted in compositional buoyant material rising, causing melting in the uppermost mantle. On the other hand, Tang et al. [2014] proposed that the mantle upwelling feeding the CBS volcano originated from below the 660km discontinuity. In this model, the hot buoyant sub-lithospheric mantle that has been entrained beneath the sinking lithosphere of the Pacific Plate is now escaping through a gap in the subducting slab caused by the subduction process. This model relies on a gap opening within subducting slab at depth to allow for a focused upwelling. The cause of the gap is still uncertain but may depend on the local sinking of the stagnant slab at the base of the upper mantle or the dynamics of slab descent through the transition zone [Tang et al., 2014].

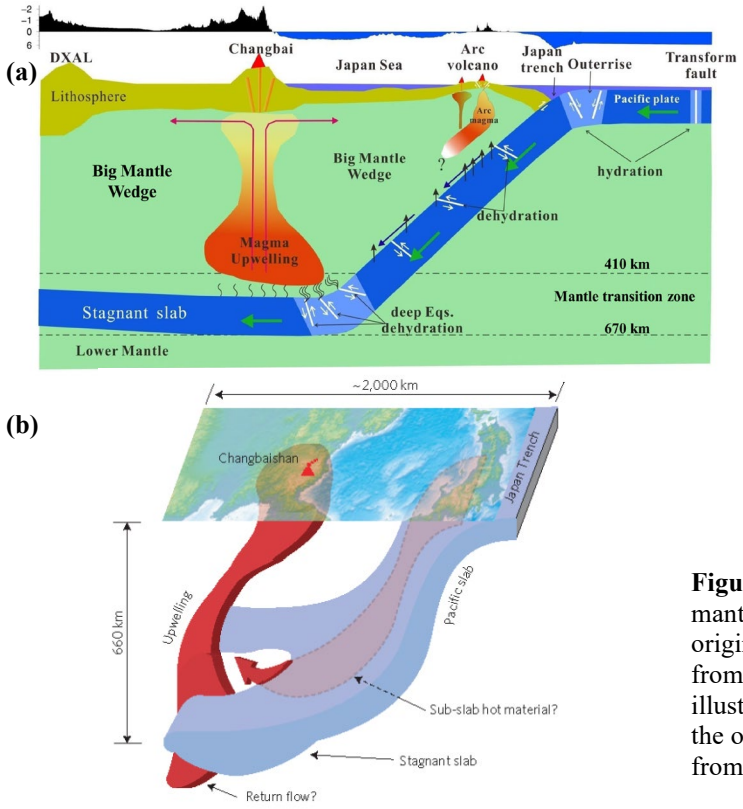


**Figure 2**. (a) A cartoon illustrating the "big mantle wedge" model associated with the origin of CBS volcano. This figure is taken from Zhao and Tian [2013]. (b) A cartoon illustrating the "gap" model associated with the origin of CBS volcano. This figure is taken from Tang et al. [2014].

Although these models explaining CBS magmatism differ in many essential aspects, similar subduction-related scenarios predict anomalies in the upper mantle and crust and potential magma reservoir beneath CBS volcanoes. Many geophysical studies have been made to probe the underlying structure of CBS, including the magnetotelluric measurements [Qiu et al., 2014; Tang et al., 2001], wide-angle reflection and refraction using controlled sources [Zhang et al., 2002; Liu et al., 2005; Song et al., 2007], attenuation [Wu et al., 2006], receiver functions [Hetland et al., 2004; Tao et al., 2014; Ri et al., 2016; Wu et al., 2009; Zhu et al., 2019; Hammond et al., 2020],

surface waves [Li et al., 2012; Kim et al., 2017; Yang et al., 2019; Zhu et al., 2019], and teleseismic tomography [Lei and Zhao, 2005; Huang and Zhao, 2006]. These studies using multidisciplinary approaches have identified zones of high conductivity, high attenuation, and low seismic velocity, which were interpreted as indicators of partial melt and/or high temperatures in the crust beneath CBS. We briefly reviewed some studies in the next section.

## 1.2 Review of Previous Studies about the CBS Volcano

Huang and Zhao [2006] obtained a high-resolution P-wave velocity tomographic model of the crust and mantle under China and surrounding regions using about one million P-wave travel times of teleseismic events. Under the intraplate CBS volcanic areas, low-velocity zones exist from the surface down to 200-300km depth, right above the mantle wedge of the Pacific subduction slab (Figure 3). Similarly, a regional P-wave velocity tomography generated using teleseismic events data [Lei and Zhao, 2005] also showed low-velocity zones beneath the CBS volcanic areas (Figure 4). The low-velocity zones extend to an even deeper depth approaching the 410km discontinuity. The P and S tomography images for NE China obtained by Tang et al. [2014] using waveforms recorded at NECESSArray (YP in Figure 11) and CNDSN stations (HL, JL, and LN in Figure 11) clearly showed a cylinder-shaped low-velocity anomaly from right below CBS down to 700km (Figure 5).

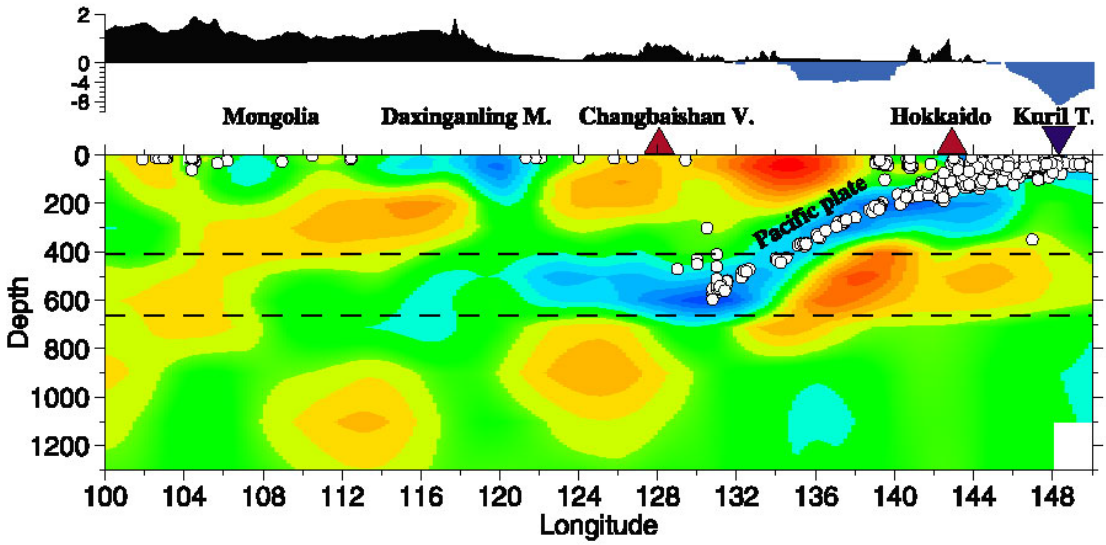


**Figure 3**. Vertical cross-sections of P wave velocity perturbations along with the profile across the CBS. The white dots indicate earthquakes, the red triangles denote volcanoes, and the dark inverted triangle denotes the Kurl trench. The scale of velocity perturbation is from -2% (red) to 2% (blue). This figure is taken from Figure 8 in Huang and Zhao [2006].

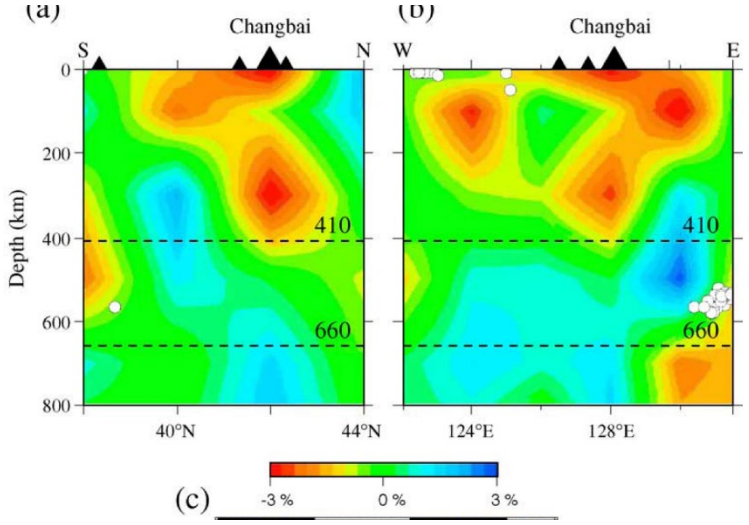


**Figure 4**. N-S (a) and E-W (b) vertical cross-sections of P wave velocity perturbations across the CBS. The white dots indicate earthquakes, and the black triangles denote the CBS volcano. This figure is taken from Figure 10 in Lei and Zhao [2005].

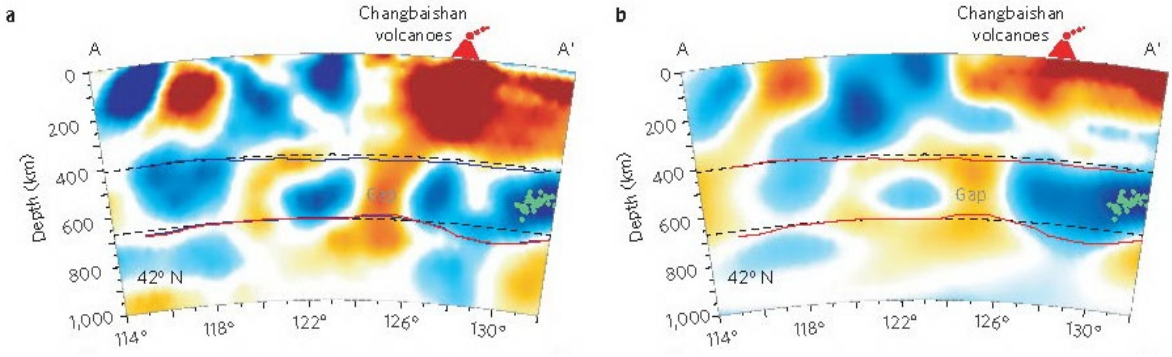


**Figure 5**. S wave (left panel) and P wave (right panel) velocity perturbations across the CBS. Fast and slow anomalies are indicated by blue and red colors, respectively. Green dots denote deep earthquakes. This figure is taken from Figure 3 in Tang et al. [2014].

The major difference between these tomographic models is in the lower mantle. Lei and Zhao [2005] model does not show apparent low-velocity anomalies in the lower mantle (Figure 4). Huang and Zhao [2006] model does show a low-velocity block in the lower mantle, but it is separated from the upper mantle low-velocity zone by the stagnant slab of Pacific subduction (Figure 3). In the model of Tang et al. [2014], the anomaly extends from just below 660 km depth to the surface through a gap in the stagnant subducted Pacific Plate (Figure 5). Differences between these models lead to the "big mantle wedge" model and the "gap" model to explain the origin of CBS volcanism (Figure 2). Nevertheless, the low-velocity anomalies in the upper mantle revealed by these studies are a manifestation of mantle upwelling that results in decompression melting to produce the observed CBS volcanic magmatism. Due to the limited resolution of these velocity images, however, these models could not confirm the existence of magma reservoirs containing molten material in the crust or upper mantle. Instead, the structure of the crust and upper mantle is usually determined by studies using multiple data sets such as receiver functions, controlled source, and surface waves/seismic noise interferometry.

As the first-order crustal properties, the crustal thickness ($H$) and bulk crustal Vp/Vs ratio ($\kappa$) beneath the CBS volcano have been estimated in many studies. Applying the $H$-$\kappa$ analysis on receiver function data recorded at the seismic deployment of "Study of Changbai Volcanoes and Deep Subduction Zone" (XI in Figure 11), Hetland et al. [2004] resolved a crustal thickness of 30–39km under the volcanic region and 28–32 km away from the volcanic region, with a mid-crust velocity transition at about 10–15 km depth. Using the same data set of XI but by inverting for S-wave profiles from receiver functions, Duan et al. [2005] revealed that the crustal thickness under the crater of the CBS volcano (Tianchi) reaches about 36km. Using the seismic deployment of "Mt. Paektu Seismic Network" (1U in Figure 7), Hammond et al. [2020] resolved a thicker crust (up to 40km) beneath the volcano (Figure 6a). Zhu et al. [2019] also obtained the same result by performing $H$-$\kappa$ analysis on different datasets. We plot a 2D relief map showing the crustal thickness in a larger area in NE China surrounding the CBS in Figure 7a. The crustal thickness data are taken from the $H$-$\kappa$ search results of (1) Chen and Niu [2016] on the permanent stations in NE China, (2) Hetland et al. [2004] on the temporal network XI, and (3) Ri et al. [2016] and Hammond et al. [2020] on the temporal network 1U. We make use of the results of these studies because we own the $H$-$\kappa$ data [Chen and Niu, 2016] or the $H$-$\kappa$ data are tabled in the individual research papers. The 2D map is interpolated using the ordinary Kriging method with minimum smoothness [Chen and Niu, 2016]. The crust beneath the CBS volcano has a thickness of 37 – 38km, about 5km thicker than the crust ~50km away from the volcanic area. Not only the studies using receiver functions [Hetland et al., 2004; Ri et al., 2016; Hammond et al., 2019], but the other studies using multiple data sets such as controlled sources [Liu et al., 2005; Song et al., 2007; Zhang et al., 2002] and surface waves/seismic noise interferometry [Zhu et al., 2019] also reveal a thicker crust presenting beneath the volcano compared to surrounding regions although they may disagree on aspects of the internal crustal structure. A thicker crust is often found beneath volcanic areas linked to the intrusion of mafic material into the lower crust.

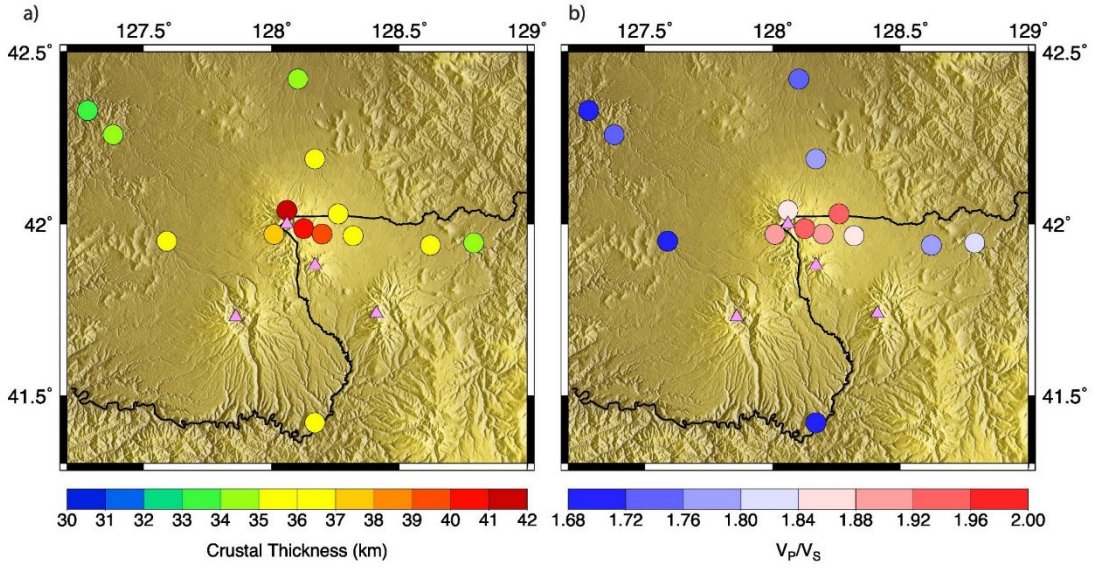


**Figure 6**. Map of (a) crustal thickness and (b) Vp/Vs ratio around the CBS volcano. The solid circles indicate stations in network 1U. The values of crustal thickness and Vp/Vs ratio derived from individual stations are represented by the colors of solid circles. This figure is taken from Figure 3 in Hammond et al. [2020].

The Vp/Vs ratio estimated by Ri et al. [2016] increases approximately 20 km from the volcano, rising to >1.87 directly beneath the volcano. Hammond et al. [2020] analyzed more data on the

deployment 1U than Ri et al. [2016] did and found that the Vp/Vs ratio could be as high as 1.93 beneath the volcano (Figure 6b). The estimates of Vp/Vs are more ambiguous than the estimates of crustal thickness. Hetland et al. [2004] inferred Vp/Vs ratios range between 1.63 and 1.87 for the bulk of the crust but suggested that Vp/Vs ratios were lower in central volcanic regions than in surrounding regions. We use the same source dataset and methodology as the crustal thickness map to create a 2D Vp/Vs map for a larger area around the CBS (Figure 7b). In a region centered at the CBS crater with a ~50km radius, the Vp/Vs ratio is generally higher than 1.80, rising to > 1.85 directly beneath the CBS crater. Because only one station (PDBD) used in Figure 6b has Vp/Vs ratio approaching 1.93 [Hammond et al., 2020], this high value is mitigated during the interpolation process used for Figure 7b.

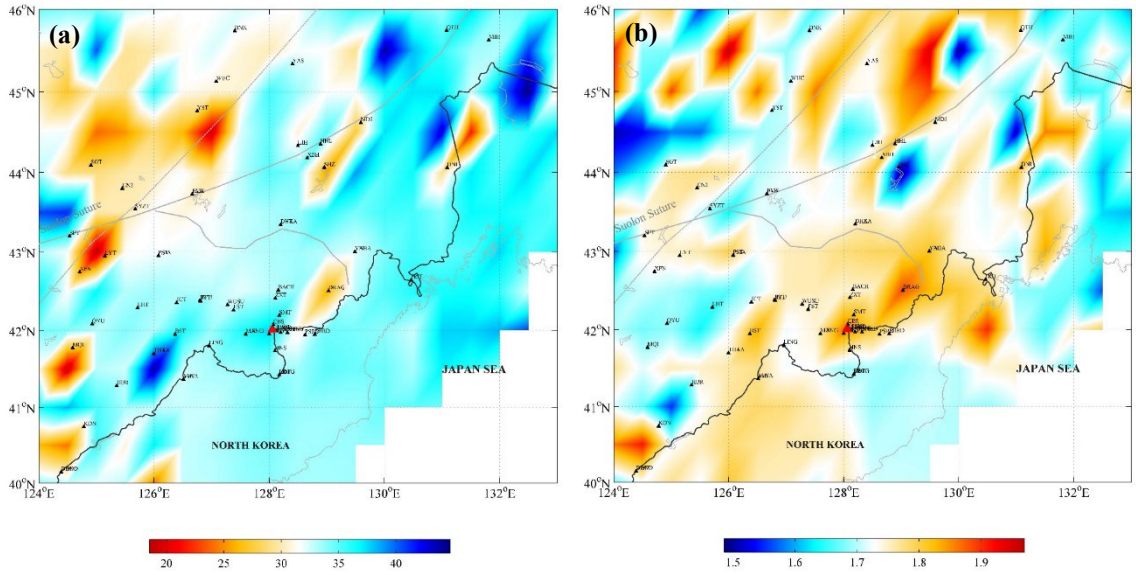


**Figure 7**. 2D relief maps for crustal thickness **(a)** and average crustal Vp/Vs ratio **(b)** around the CBS volcanic area derived from the results of H-κ analysis on receiver function data. The 2D maps are interpolated from station measurements using the ordinary kriging method.

The increased crustal thickness and Vp/Vs ratio show that a large crust region around the CBS volcano has been modified by magmatism associated with the volcanism. These features indicate an upwelling channel of the asthenospheric material with a high mafic composition. The mafic intrusion attaches to the bottom of the crust and thus deepens the Moho beneath the volcano. However, a high mafic composition is not sufficient to explain Vp/Vs ratios higher than 1.87. Such a high Vp/Vs value indicates partial melting in the crust below the CBS. This melt region represents a potential source of magma that erupted over the past few thousand years and was likely related to the volcanic unrest episode between 2002 and 2005. However, the crustal average Vp/Vs ratios do not identify the potential magma reservoir/chamber in the crust or determine the location and size of the magma reservoir.

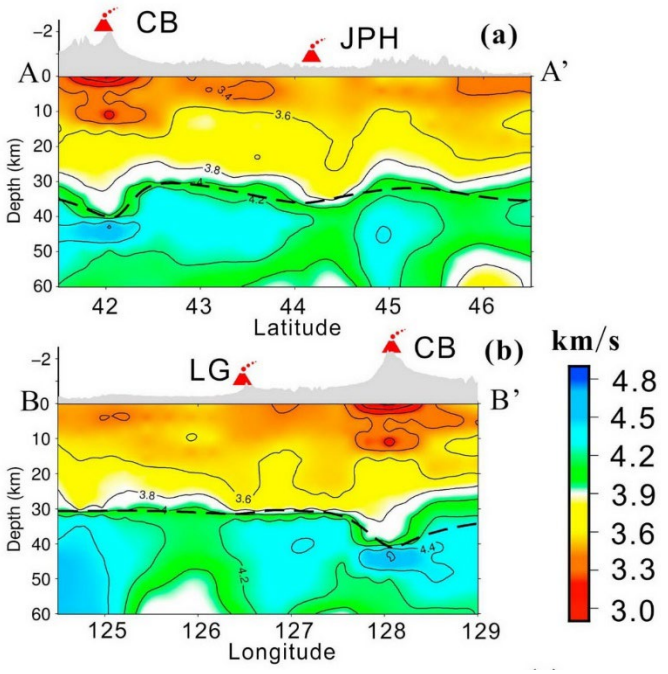


**Figure 8**. Vertical cross-sections of S wave velocity tomography across the CBS. The red triangles denote volcanoes. The black dash line denotes the Moho discontinuity estimated from the receiver-function stacking. This figure is taken from Figure 11 in Zhu et al. [2019].

Hetland et al. [2004] resolved a low-velocity anomaly extending from about 5–10 to 15–25 km below the surface, indicating a region of elevated temperatures. However, they were unable to determine whether partial melting was present based on the data used in their study. Wu et al. [2009] inverted a 1D S-wave velocity model using the receiver function data on a station near the CBS crater. Their model showed a low-velocity layer at 8km extending to 28km with the lowest S-wave velocity of ~2.2 km/s. Such a low velocity indicates the existence of the high-temperature material or magma reservoir in the crust beneath the CBS volcano. While at a station located 50km north of the crater, Wu et al. [2009] detected no obvious crustal low-velocity layer, suggesting the magma reservoir extended less than 50km laterally. The common conversion point migrations performed by Hammond et al. [2020] on the receiver function data recorded at deployment 1U also detected a low-velocity zone extending ~30km deep from the volcano summit. This low-velocity zone corresponds to a melt-rich region with the top found 4-8km below sea level, with the shallowest depth directly beneath the volcano. The base of this melt-rich region could not well be constrained, suggesting melt is pervasive throughout the crust. On the other hand, the low-velocity zone determined by a joint inversion of surface wave and receiver functions extended to ~100km in the north and south directions from the CBS volcano laterally [Zhu et al., 2019]. Although the depth of the low-velocity zone beneath the volcano determined by Zhu et al. [2019] is 8 – 15 km (Figure 8), similar to that determined by Hetland et al. [2004] and Hammond et al. [2019], the lateral extent revealed by Zhu et al. [2019] is much broader than the results of the other two studies, implying a more extensive magma reservoir in the mid crust. The joint inversion of surface wave and receiver functions performed by Chen and Niu [2016] on the permanent stations also revealed low-velocity zones in the mid-crust and lower-crust beneath the CBS volcano (Figure 9); however, the S-velocity value of low-velocity zone is not as low as that resolved in Zhu et al. [2019].

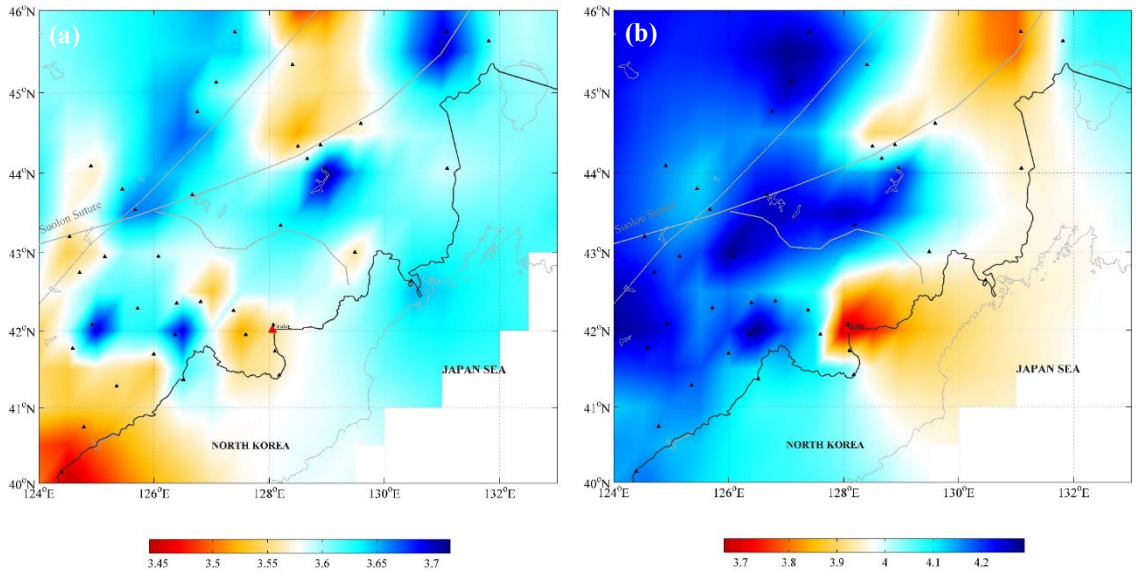


**Figure 9**. 2D relief maps for S-velocities at **(a)** 14km and **(b)** 35km. The S-velocities of individual stations are taken from the joint inversion of surface wave and receiver functions performed by Chen and Niu [2016]. The 2D maps are interpolated from station measurements using the ordinary kriging method.

## 1.3 Purposes of This Study

These previous studies revealed thickened crust, high bulk crustal Vp/Vs ratio, and low-velocity zone in the mid-crust beneath the CBS volcano, suggesting partial melting of the mid-crust. The partial melting is likely related to a magma reservoir in the mid-crust. These results support the hot and wet asthenosphere mantle upwelling driven by the subduction of the Pacific Plate, regardless of the origin of asthenospheric materials. Due to the resolving capability of the seismic techniques and data used in these studies, considerable discrepancies can be found in their results. For example, the inherent trade-off between $H$ and $\kappa$ in the $H$-$\kappa$ analysis may yield two pairs of $H$ and $\kappa$, one with a higher $H$ value and lower $\kappa$ value and the other with a lower $H$ value and higher $\kappa$ value. Special inspection combining geological knowledge is required in a region with complex crustal structures to identify the appropriate results [Ri et al., 2016]. Moreover, as the average crustal Vp is a free parameter in $H$-$\kappa$ analysis, choosing different Vp values also affects the results.

Conceptually, if a magma reservoir exists underneath a volcano, the S-wave can not penetrate the magma reservoir/chamber, while the penetrating P-wave will be delayed. In the study of the Tatun volcano group (TVG) in northern Taiwan, Lin [2016] observed significant S-wave shadows and P-wave delays in the seismograms of deep-focus earthquakes beneath the TVG recorded at the densely deployed seismic stations at the TVG. S-wave shadows and P-wave delays are direct evidence of a deep magma reservoir beneath the TVG when seismic waves propagate through the magma reservoir. As the Northern Taiwan Volcanic Zone is not likely a part of the typical volcanic arc induced directly by the subduction process, the magma reservoir beneath the TVG might be the result of some degree of melting within an ascending region of the asthenosphere mantle. The station observations indicated that the molten magma might exist in either the lower crust or the upper mantle along the ray paths from earthquakes to particular stations. Using a ray tracing method on a simplified 1D model with a low-velocity zone (-40%) in the lower crust, Lin [2016] further estimated the location and size of the magma reservoir from calculated ray paths and travel

times. The reasonable estimation of its depth might be at the lower crust but not in the upper mantle because an extremely low velocity is required to cause observed P-wave delays of ~0.4s, and the maximum size of the magma reservoir might be 15km × 6km.

The CBS volcanos are located in an area with densely distributed seismic stations and abundant deep and shallow earthquakes. Many deep-focus earthquakes occurred within the Wadati-Benioff seismic zone of the subducting Pacific slab. The seismic rays of these deep earthquakes traveling stations in NE China will thoroughly scan the areas beneath the CBS volcano. It thus provides us with the opportunity to directly detect the potential CBS magma reservoir by applying a technique similar to Lin [2016] and Lin et al. [2018]. We detected magma reservoirs by seeking S-wave shadows and P-wave delays from the seismograms recorded at dense stations in NE China. And then, we performed ray tracing simulations to characterize the magma structure. The results of previous studies would be used to construct reference models for our ray tracing calculations.

# 2 SEISMIC DATA AND DATA PROCESSING

## 2.1 Selection of Deep-Focus Earthquakes

From NE China to Japan Trench is an area with a relatively high seismicity rate, including a large number of shallow-focus earthquakes that occurred within the crust (depth < ~35km) and deep-focus earthquakes that occurred at depths of 100 – 600km (Figure 10). The grouped activities of shallow-focus and deep-focus earthquakes in NE China more or less are related to the collision between the west Pacific plate and the Eurasian plate, as well as the form of the subduction of the Pacific plate [e.g., Sun and He, 2004; Zhu et al., 2010]. All deep-focus earthquakes occur within the Wadati-Benioff seismic zone of the subducting Pacific slab beneath the Japan Sea and the northeastern Eurasian continent margin.

According to the availability of waveform data on our selected stations, we judiciously selected 97 deep-focus earthquakes from 1996 to 2017 near the CBS volcanic area (solid red circles in Figure 10). Along with the subducting direction of the Pacific slab, earthquakes at ~100km deep occur in the Japan Sea, about 1000km from the CBS area horizontally. The earthquakes at 410 – 660km deep are located directly beneath the CBS volcano, concentrating on the stagnant Pacific slab in the mantle transition zone. Because the deep earthquakes that occurred at various depths propagate along different paths to arrive at the same stations, the behaviors of observed P- and S-wave will help constrain the location and size of the magma reservoir. Among the 97 deep earthquakes, there are 73 with a minimum magnitude of 4.5. We also exploited smaller earthquakes if some stations within a short distance captured them. The redundancy of selected earthquakes ensures sufficient seismic data for our study. The source information of these selected events is summarized in Table 1.

These deep-focus earthquakes are good seismic sources to detect the magma reservoir beneath CBS volcanoes. It is worth noting that some earthquakes are clustered, such as 1996.03.13_00.47.419, 1999.03.02_09.38.472, 2011.04.29_07.13.120, 2011.05.29_05.46.428, and 2011.06.07_17.02.085 (Table 1). The relative hypocenters of these earthquakes are within 30km.

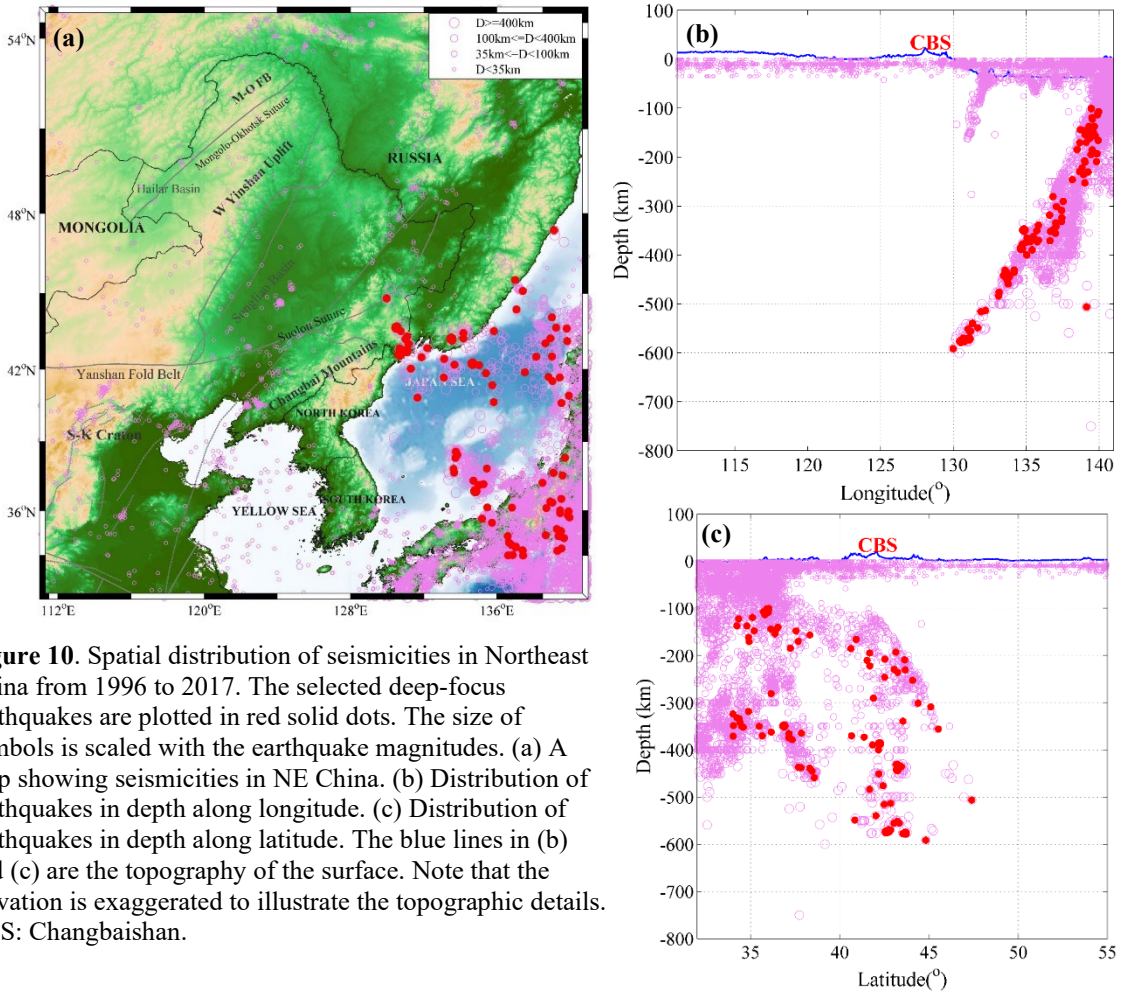


**Figure 10**. Spatial distribution of seismicities in Northeast China from 1996 to 2017. The selected deep-focus earthquakes are plotted in red solid dots. The size of symbols is scaled with the earthquake magnitudes. (a) A map showing seismicities in NE China. (b) Distribution of earthquakes in depth along longitude. (c) Distribution of earthquakes in depth along latitude. The blue lines in (b) and (c) are the topography of the surface. Note that the elevation is exaggerated to illustrate the topographic details. CBS: Changbaishan.

Table 1: Source Information of Selected Deep-focus Earthquakes

| Origin time | Lat (°) | Lon (°) | Depth (km) | Mag | Event ID | Recording Networks |
|---|---|---|---|---|---|---|
| 1996- 1-30 21 14 56.52 | 36.1478 | 135.4776 | 362.3 | 4.87 mb | 1996.01.30_21.14.565 | XL |
| 1996- 7-24 0 50 14.45 | 34.2366 | 137.4116 | 332.0 | 4.64 mb | 1996.07.24_00.50.145 | XL |
| 1996-10-30 9 9 41.79 | 41.6837 | 138.8225 | 222.0 | 5.26 mb | 1996.10.30_09.09.418 | XL |
| 1996-11-25 0 26 38.50 | 38.4323 | 133.8347 | 444.8 | 4.56 mb | 1996.11.25_00.26.385 | XL |
| 1996-12- 3 15 49 14.33 | 37.5435 | 139.5868 | 147.9 | 5.20 mb | 1996.12.03_15.49.143 | XL |
| 1996-12-22 14 53 29.25 | 43.2387 | 138.9306 | 235.5 | 5.97 mb | 1996.12.22_14.53.293 | XL |
| 1998- 6-16 20 10 0.95 | 34.7933 | 139.6700 | 137.2 | 4.68 mb | 1998.06.16_20.10.010 | XI |
| 1998- 8-20 9 36 35.75 | 45.5208 | 136.9960 | 355.8 | 5.22 mb | 1998.08.20_09.36.358 | XI |
| 1999- 4- 8 13 10 35.60 | 43.6690 | 130.5061 | 576.5 | 6.39 mb | 1999.04.08_13.10.356 | XI |
| 1999- 4-18 23 14 20.20 | 34.3236 | 139.5332 | 122.4 | 4.84 mb | 1999.04.18_23.14.202 | XI |
| 1999- 8- 8 21 39 38.80 | 35.8046 | 139.8837 | 113.6 | 4.70 mb | 1999.08.08_21.39.388 | XI |
| 1999-10- 1 3 47 22.93 | 37.6635 | 139.1043 | 170.0 | 4.52 mb | 1999.10.01_03.47.229 | XI |
| 1999-10- 3 4 6 46.08 | 35.6520 | 135.1809 | 370.0 | 4.58 mb | 1999.10.03_04.06.461 | XI |
| 1999-12- 5 7 28 33.21 | 42.5143 | 139.0081 | 207.8 | 4.80 mb | 1999.12.05_07.28.332 | XI |
| 1999-12-31 13 9 12.98 | 37.3216 | 134.7162 | 378.3 | 5.04 mb | 1999.12.31_13.09.130 | XI |
| 2006- 2- 1 11 35 53.75 | 35.7145 | 139.9657 | 107.1 | 4.79 mb | 2006.02.01_11.35.538 | V0 |
| 2006- 4-24 4 28 14.93 | 38.3111 | 139.7299 | 156.4 | 4.71 mb | 2006.04.24_04.28.149 | V0 |
| 2006- 5-10 16 47 50.79 | 43.6323 | 139.8185 | 209.3 | 4.89 mb | 2006.05.10_16.47.508 | V0 |

| | | | | | | |
|---|---|---|---|---|---|---|
| 2006- 9-16 2 22 50.96 | 41.3524 | 135.7497 | 373.0 | 5.12 mb | 2006.09.16_02.22.510 | V0 |
| 2006-11-27 19 26 5.70 | 37.6686 | 133.6624 | 436.2 | 4.70 mb | 2006.11.27_19.26.057 | V0 |
| 2009- 1-22 0 9 34.34 | 40.9160 | 139.9378 | 165.6 | 4.73 mb | 2009.01.22_00.09.343 | YP |
| 2009- 1-22 12 21 0.71 | 34.2208 | 139.3105 | 137.0 | 4.73 mb | 2009.01.22_12.21.007 | YP |
| 2009- 1-26 8 54 21.87 | 36.5283 | 139.5196 | 139.7 | 4.51 mb | 2009.01.26_08.54.219 | YP |
| 2009- 3-13 9 7 1.93 | 43.2398 | 134.1631 | 430.5 | 4.83 mb | 2009.03.13_09.07.019 | YP |
| 2009- 4-18 3 56 31.38 | 42.8457 | 130.6792 | 569.5 | 4.77 mb | 2009.04.18_03.56.314 | YP |
| 2009- 6-10 4 7 2.73 | 34.5810 | 136.6598 | 351.6 | 4.53 mb | 2009.06.10_04.07.027 | YP |
| 2009- 7-16 6 29 4.44 | 42.4150 | 133.1157 | 476.1 | 4.91 mb | 2009.07.16_06.29.044 | YP |
| 2009- 8-10 12 42 53.15 | 43.5266 | 130.7373 | 577.1 | 4.81 mb | 2009.08.10_12.42.532 | YP |
| 2009-11-15 20 31 34.56 | 44.3784 | 137.0688 | 301.1 | 4.69 mb | 2009.11.15_20.31.346 | YP |
| 2009-12-24 0 23 32.25 | 42.1656 | 135.0247 | 400.0 | 5.12 mb | 2009.12.24_00.23.323 | YP |
| 2009-12-24 0 23 33.38 | 42.2277 | 134.6670 | 386.8 | 6.02 mb | 2009.12.24_00.23.334 | YP; HL; JL: LN |
| 2010- 2- 5 6 48 10.25 | 40.6537 | 135.8279 | 370.1 | 4.93 mb | 2010.02.05_06.48.103 | YP; |
| 2010- 2-18 1 13 18.35 | 42.5934 | 130.6807 | 573.9 | 6.16 mb | 2010.02.18_01.13.184 | YP; HL; JL; LN |
| 2010- 4-29 15 19 9.66 | 37.1389 | 135.0504 | 365.1 | 4.60 mb | 2010.04.29_15.19.097 | YP; |
| 2010- 8-26 15 8 4.94 | 36.1401 | 136.8238 | 280.7 | 5.09 mb | 2010.08.26_15.08.049 | YP; |
| 2010- 9-21 20 15 10.08 | 40.6143 | 139.5297 | 185.2 | 4.66 mb | 2010.09.21_20.15.101 | YP; |
| 2011- 1- 7 23 34 10.64 | 43.0290 | 131.1629 | 555.3 | 4.77 mb | 2011.01.07_23.34.106 | YP; HL; JL; LN |
| 2011- 5-10 15 26 5.05 | 43.3199 | 131.0913 | 554.9 | 5.34 mb | 2011.05.10_15.26.051 | YP; HL; JL; LN |
| 2011-12-14 7 48 44.48 | 42.5060 | 138.1551 | 245.8 | 4.64 mb | 2011.12.14_07.48.445 | YP; |
| 2013- 4- 5 13 0 2.36 | 42.7359 | 131.0640 | 571.3 | 6.16 mb | 2013.04.05_13.00.024 | HL; JL; LN |
| 2013- 4- 6 0 29 55.51 | 42.7356 | 131.0457 | 572.3 | 5.38 mb | 2013.04.06_00.29.555 | HL; JL; LN |
| 2013- 4-14 1 22 4.51 | 36.0253 | 139.4564 | 100.7 | 4.66 mb | 2013.04.14_01.22.045 | HL; JL; LN |
| 2013- 9- 2 2 51 13.21 | 42.1874 | 133.6783 | 450.5 | 5.46 mb | 2013.09.02_02.51.132 | 1U |
| 2013- 9-11 7 11 31.98 | 43.1307 | 139.8445 | 192.9 | 4.83 mb | 2013.09.11_07.11.320 | 1U |
| 2013- 9-27 18 36 41.39 | 43.4515 | 134.1685 | 435.3 | 4.67 mb | 2013.09.27_18.36.414 | 1U |
| 2013- 9-30 0 11 54.90 | 43.0402 | 138.6556 | 229.2 | 4.71 mb | 2013.09.30_00.11.549 | 1U |
| 2013-10-29 20 17 50.09 | 43.2148 | 131.0068 | 551.2 | 4.97 mb | 2013.10.29_20.17.501 | 1U |
| 2013-11-12 11 36 3.89 | 41.6686 | 139.4386 | 194.7 | 4.64 mb | 2013.11.12_11.36.039 | 1U |
| 2013-11-18 19 10 45.72 | 34.3653 | 137.0281 | 334.2 | 5.24 mb | 2013.11.18_19.10.457 | 1U |
| 2014- 1- 1 7 4 4.31 | 41.8791 | 137.5303 | 290.5 | 4.85 mb | 2014.01.01_07.04.043 | HL; JL; LN |
| 2014- 1-11 3 56 48.46 | 43.6640 | 139.2354 | 230.4 | 5.04 mb | 2014.01.11_03.56.485 | HL; JL; LN |
| 2014- 2-20 1 32 51.73 | 42.8482 | 132.1958 | 513.4 | 4.53 mb | 2014.02.20_01.32.517 | HL; JL; LN |
| 2014- 5- 4 20 18 25.01 | 34.8781 | 139.3660 | 161.4 | 5.76 mb | 2014.05.04_20.18.250 | HL; JL; LN |
| 2014- 5-15 9 48 13.46 | 35.0993 | 139.5026 | 119.1 | 4.53 mb | 2014.05.15_09.48.135 | HL; JL; LN |
| 2014- 6-28 5 51 5.60 | 36.3617 | 139.0394 | 153.8 | 4.51 mb | 2014.06.28_05.51.056 | HL; JL; LN |
| 2014-12- 5 16 1 56.43 | 35.4731 | 135.7285 | 350.1 | 4.61 mb | 2014.12.05_16.01.564 | HL; JL; LN |
| 2015- 1-19 22 34 48.98 | 37.2277 | 138.4885 | 184.7 | 4.80 mb | 2015.01.19_22.34.490 | HL; JL; LN |
| 2015- 2- 7 16 40 5.27 | 43.5318 | 135.8359 | 339.2 | 4.58 mb | 2015.02.07_16.40.053 | HL; JL; LN |
| 2015- 4-12 6 25 14.67 | 36.4120 | 138.9224 | 145.7 | 4.53 mb | 2015.04.12_06.25.147 | HL; JL; LN |
| 2015- 5- 3 14 30 15.92 | 36.1261 | 138.7045 | 143.9 | 4.81 mb | 2015.05.03_14.30.159 | HL; JL; LN |
| 2015- 5-25 6 37 40.72 | 41.8428 | 135.4000 | 389.7 | 4.87 mb | 2015.05.25_06.37.407 | HL; JL; LN |
| 2015-11- 7 13 44 44.50 | 35.9826 | 139.9191 | 108.7 | 5.09 mb | 2015.11.07_13.44.445 | HL; JL; LN |
| 2016- 1- 2 4 22 19.26 | 44.8106 | 129.9676 | 591.3 | 5.70 mb | 2016.01.02_04.22.193 | HL; JL; LN |
| 2016- 1-18 0 56 46.92 | 35.1955 | 139.2737 | 147.6 | 4.57 mb | 2016.01.18_00.56.469 | HL; JL; LN |
| 2016- 7-17 9 43 24.78 | 34.4010 | 137.0381 | 342.0 | 4.68 mb | 2016.07.17_09.43.248 | HL; JL; LN |
| 2016-11-11 4 53 37.44 | 34.4864 | 136.7937 | 349.7 | 4.65 mb | 2016.11.11_04.53.374 | HL; JL; LN |
| 2017- 1-12 17 4 57.77 | 41.6636 | 133.0924 | 483.7 | 5.03 mb | 2017.01.12_17.04.578 | HL; JL; LN |
| 2017- 2-15 19 41 0.63 | 37.1673 | 135.2676 | 372.7 | 4.57 mb | 2017.02.15_19.41.006 | HL; JL; LN |
| 2017- 3-20 8 22 28.04 | 44.0705 | 139.0117 | 252.6 | 4.50 mb | 2017.03.20_08.22.280 | HL; JL; LN |
| 2017- 4-12 7 34 59.47 | 38.5718 | 133.7558 | 458.9 | 4.57 mb | 2017.04.12_07.34.595 | HL; JL; LN |
| 2017- 6-13 23 37 33.11 | 37.1301 | 134.9809 | 374.0 | 4.51 mb | 2017.06.13_23.37.331 | HL; JL; LN |

| | | | | | | |
|---|---|---|---|---|---|---|
| 2017- 7-12 19 48 7.37 | 40.8368 | 131.6599 | 548.7 | 5.87 mb | 2017.07.12_19.48.074 | HL; JL; LN |
| 2017-11-30 9 18 23.60 | 38.3084 | 133.7282 | 438.9 | 5.18 mb | 2017.11.30_09.18.236 | HL; JL; LN |

## 2.2 Seismic Stations in NE China

Many temporal seismic stations have been deployed around the CBS volcanic region to study this volcano. The temporal seismic deployments selected for this study include Mt. Paektu Seismic Network (1U in Figure 11), Study of Changbai Volcanoes and Deep Subduction Zone (XI in Figure 11), North Korea Nuclear Site Investigation (XL in Figure 11), Northeast China Extended Seismic Array (YP in Figure 11), and one deployment belonging to Chinarray (V0 in Figure 11). These temporal stations were usually operated from several months to several years. They may not be able to capture sufficient seismic events to satisfy our requirements. For example, the open information from Chinarray claimed that the operation period of V0 was from 2006 to 2008, but we only obtained the seismograms of four earthquakes (Table 1). For this reason, we also selected permanent stations in NE China: Heilongjiang (HL), Jilin (JL), and Liaoning (LN) (Figure 11). Each of these three regional seismic networks consists of ~50 stations that have been updated from analog stations or established since 2009. These regional seismic networks are part of the Chinse National Digital Seismic Network (CNDSN), and their waveform data are archived in the Chinese Earthquake Network Center (CENC). We downloaded the waveform data of PASSCAL-type seismic deployments from IRIS-DMC. We retrieved the waveform data of CNDSN and V0 from CENC and the Institute of Geophysics, CEA, respectively, through the collaboration program between ARRAY and Chinese collaborators.

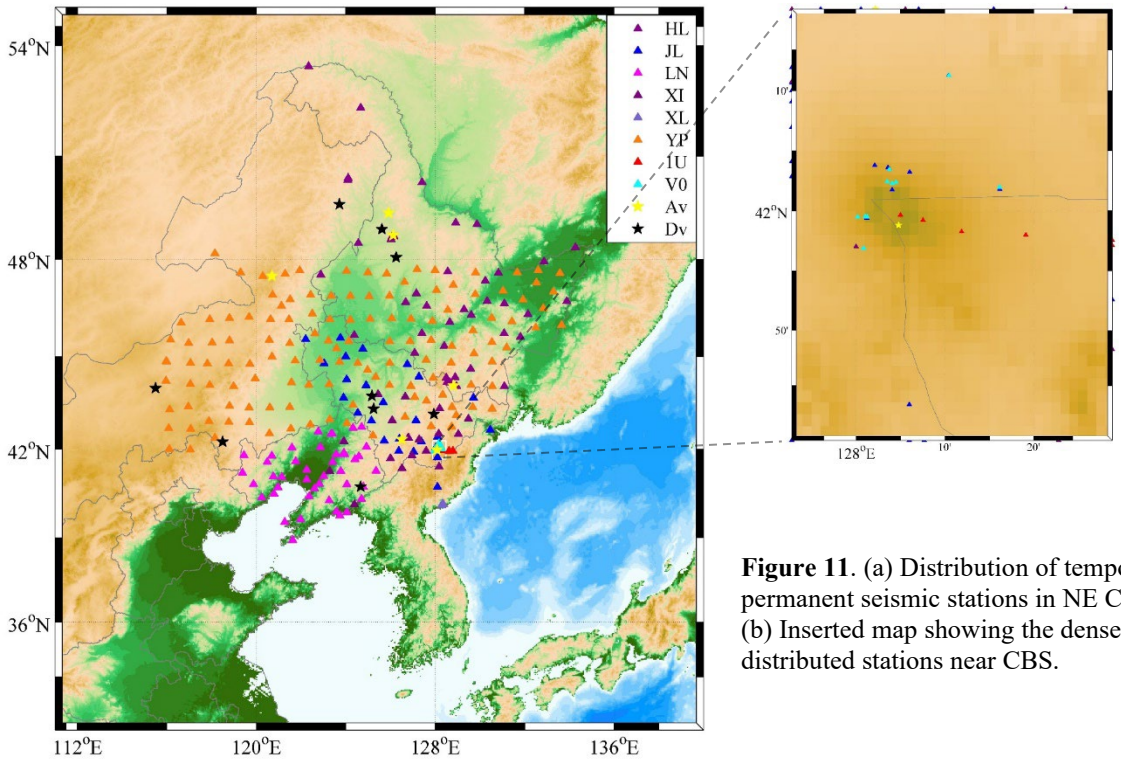


**Figure 11**. (a) Distribution of temporal and permanent seismic stations in NE China. (b) Inserted map showing the densely distributed stations near CBS.

Some ad hoc seismic deployments were specifically designed to study CBS volcanoes, such as 1U and V0. As shown in the inserted map of Figure 11b, these stations are densely deployed around the CBS volcano. If observed at these stations, the S-wave shadows and P-wave delays of

deep earthquakes will demonstrate the presence of melting or extremely low anomalies beneath the CBS volcano.

## 2.3 Picking P- and S-wave Arrivals

We manually picked P- and S-arrivals on each seismogram for selected earthquakes. It is a critical step because the actual P- and S-wave travel time will be compared to the predicted travel time to determine the structure below the CBS volcano through the error-and-trial or more sophisticated inverse method. We initially used two types of 1D crustal and upper mantle velocity models to predict P- and S-arrivals. The first model is AK135 global model [Kennett et al. 1995], and the second is a regional model for NE China (Figure 12). Chen and Niu [2016] obtained 1D velocity models beneath ~1000 CNDSN stations across China by joint inversion of receiver function and surface wave dispersion data. The NE China model is the average of selected 1D models of NE China stations. As the receiver function and surface wave data used by Chen and Niu [2016] have little sensitivities for the upper mantle deeper than 150km, we used the AK135 model for the mantle deeper than 150km. The upper mantle in the NE China model generally has lower Vs and Vp than the global average. The Moho depth in NE China was determined in the range of ~32 - ~35km using the receiver function data of individual stations, but it is smoothed as a transition zone in the model (Figure 12) when we averaged many individual station velocity profiles. Compared to the AK135 model, the NE China model displays a low-velocity zone in the lower crust.

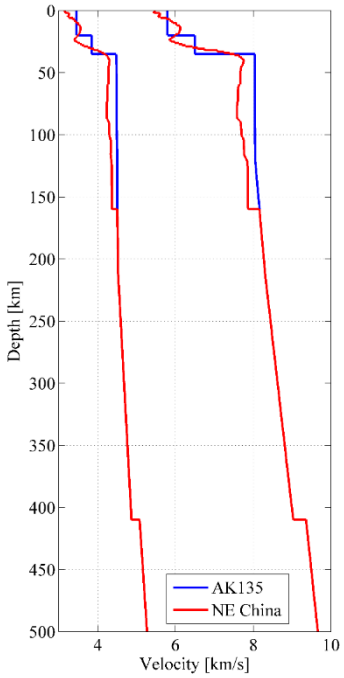


**Figure 12**. Vp and Vs models used to predict the arrivals of P and S phases. The blue lines are the global AK135 crustal and upper mantle models. The red lines are the regional models for NE China, which are averages of individual 1D models on the stations in NE China.

Figure 13 shows the three-component seismograms of event 2010.02.18_01.13.184 (Table 1) recorded at JL.BST, a station located ~200km from the CBS crater. The green and magenta bars in Figure 13 indicate the predicted P- and S-arrivals, respectively, calculated using the NE China regional models. The P-wave arrives later than the predicted arrival time. On Z-component, the S-wave is missing. On E-component, the amplitude of the S wave is weaker than that of the P-wave, but the S-wave on N-component is obvious. The energy of the S wave is mainly concentrated in low frequencies.

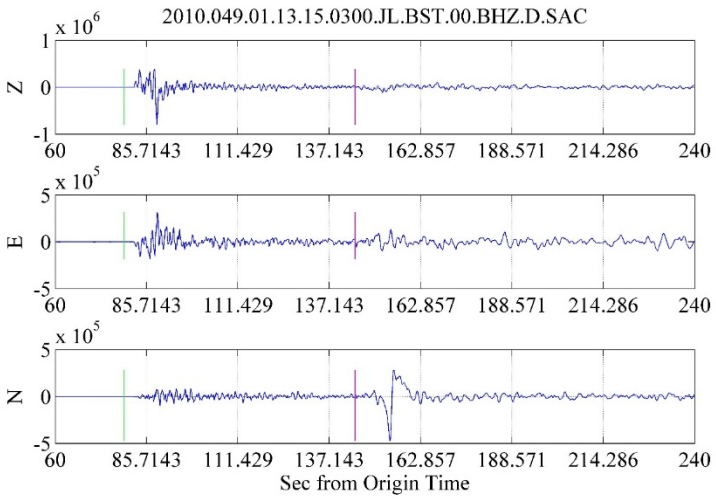


**Figure 13.** 3-components seismogram of a deep earthquake occurred on 2010-2-18, 1:13:18.35 recorded by JL.BST. The green and magenta bars indicate the predicted P- and S-arrivals, respectively, calculated using the NE China regional models.

After reviewing more seismograms in the phase-picking process, we found more typical seismograms showing S-wave shadows and P-wave delays. Figure 14 shows the seismograms of another deep earthquake 2011.01.07_23.34.106 (Table 1) recorded at JL.CBS and LN.SNY, respectively. On JL.CBS, a station at Mountain CBS, the S-wave is unidentifiable on all three components. In contrast, station LN.SNY, which is near Shenyang City in Liaoning province and far from the CBS volcanic area, clearly recorded S-wave on all components. As shown in Figure 14b, the S-wave amplitude is stronger than the P-wave (Figure 14b). We will analyze observed S-wave shadows and P-wave delays in more detail in Section 4.

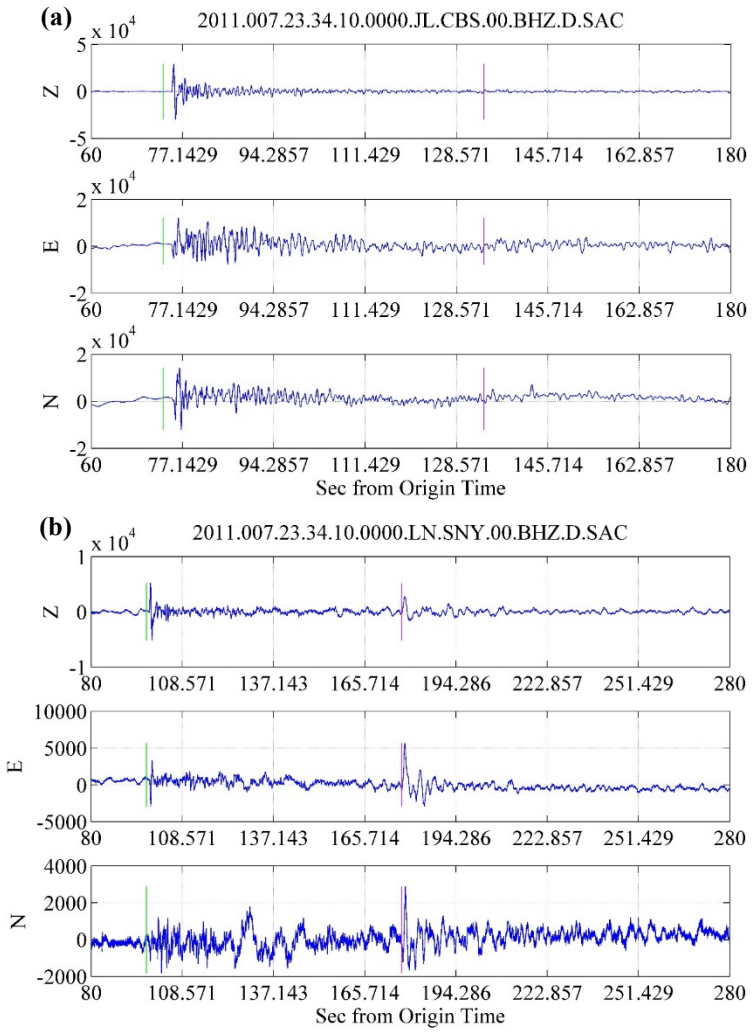


**Figure 14.** 3-components seismogram of a deep earthquake occurred at 2011-1-7, 23:34:10.64 recorded at (a) JL.CBS and (b) LN.SNY. The green and magenta bars indicate the predicted P- and S- arrivals, respectively, calculated using the NE China regional models.

# 3 METHODOLOGY

## 3.1 Complete Ray Tracing Method

Ray tracing consists of the calculation of rays, i.e., the step-by-step evaluation of the coordinates of points along the rays. The seismic ray in 3D structures can be expressed as the following second-order ordinary differential equation (ODE) governing the ray path.

$$\frac{d}{ds}\left(\frac{1}{v}\frac{d\boldsymbol{r}}{ds}\right) = \nabla\left(\frac{1}{v}\right) \tag{1}$$

where $\boldsymbol{r}$ is the spatial position vector, and $s$ is an independent variable representing the path length along the ray. The term $d\boldsymbol{r} = dx^i$, $i = 1, 2, 3$ and $\frac{d\boldsymbol{r}}{ds}$ is the tangent vector. The velocity $v(\boldsymbol{r})$ is also a function of the spatial position vector $\boldsymbol{r}$. This second-order ODE system can be reduced to a system of first-order ODEs by defining the slowness vector $\mathbf{p}(s) = \frac{1}{v}\frac{d\boldsymbol{r}}{ds}$. Then Equation (1) can be rewritten as:

$$\frac{d\boldsymbol{r}}{ds} = v\mathbf{p}, \quad \frac{d\mathbf{p}}{ds} = \nabla\left(\frac{1}{v}\right) \tag{2}$$

with six components:

$$\frac{dx^i}{ds} = vG^{ij}p_j, \frac{dp_i}{ds} = -v^{-2}\frac{\partial v}{\partial x^i} + v\Gamma_{ij}^k G^{jl}p_k p_l \quad (3)$$

where $G^{ij} = G^{ij}(x^k)$, $i, j, k = 1, 2, 3$, is the contravariant components of the metric tensor describing different coordinate systems, and $\Gamma_{ij}^k$ is the Christoffel symbols, which are the combination of covariant components $G_{ij} = G_{ij}(x^k)$ and contravariant components $G^{ij} = G^{ij}(x^k)$ of the metric tensor:

$$\Gamma_{ij}^k = \frac{1}{2}G^{kl}\left(G_{il,j} + G_{jl,i} - G_{ij,l}\right) \quad (4)$$

To keep track of the travel time $t(s)$, we may add a seventh equation:

$$\frac{dt}{ds} = \frac{1}{v} \quad (5)$$

The integral of Equation (5) yields the real-valued travel time.

In this study, we implemented ray tracing simulations using the complete ray tracing (CRT) method developed by Červeny and Klimeš [1984] and Červeny et al. [1988]. In contrast to standard ray tracing in which only the ray trajectory, travel times, and slowness vectors along the ray are determined, the CRT method consists of (a) computation of ray tracing and travel time along the ray (standard ray tracing), (b) determination of the polarization vectors along the ray, (c) dynamic ray tracing through the computation of the ray propagator matrix and (d) evaluation of the components of the reduced vectorial complex-valued amplitudes.

The output of the CRT program includes basic quantities along a ray, such as trave time, imaginary part of the complex-valued travel time ($t^*$), coordinates of points along the ray, covariant components of the slowness vector, covariant components of the polarization vector, ray propagator matrix, and complex-valued vectorial reduced amplitudes, and many auxiliary quantities. Not only the quantities along each seismic ray, but also the quantities at the interface between nearby blocks are exported for various seismological applications. At an interface, the ray is transformed following the Snell law. The CRT program is thus a powerful tool with many important seismological applications. Using the various quantities along the ray and at intersections of the ray with some selected surfaces, the CRT can be used as a basic procedure in many program packages in the numerical modeling and interpretation of high-frequency seismic wavefields in complex 3D structures with laterally varying layered and blocked structure [Červeny et al., 1988]. For example, the CRT can process ray amplitudes and paraxial ray approximation of ray amplitudes to generate synthetic body-wave seismograms.

## 3.2 Model Construction for CRT Program

The parameters used to describe the 3D model and seismic rays and to control the ray tracing calculation are organized in multiple input files. 3D ray tracing has been a longstanding challenge in computational seismology. One difficulty is dealing with the direction of wave propagation at block interfaces. In CRT, the model is implemented in a semi-descriptive way that can describe various complex structures. The model is defined inside a volume of space by smooth functions specifying the distribution of the parameters of the medium. The parameters include interfaces and blocks and the velocities and attenuation of blocks. “Smooth” means that the parameters and their first and second partial derivatives must be continuous. Because the model may contain blocks with sharp edges where their first and second partial derivatives do not exist, the algorithm uses a

special method to construct the model using two types of blocks formed by smooth surfaces: simple blocks (SBs) and complex blocks (CBs). The SBs are the "building bricks" to build the CBs, and have no physical meaning. While the CBs represent the physical units of the model. The physical parameters for the model could be P- and S-wave velocities, density, quality factors ($Q$ or attenuation) of the medium, or some powers of these quantities.

An SB is defined by the surfaces forming the boundaries of the SB. Some boundaries may also be parts of the boundaries of the model or fictitious extensions of boundaries. An SB may be formed by several separated regions, not only by one connected region. The division of a model into SBs is not unique. A point of the model may be situated in several SBs. The CBs are introduced to avoid a block being separated by fictitious surfaces. An CB is formed as a union of several SBs. Any point of the model must be situated in just one CB. The SBs and CBs are indexed by positive numbers, starting from 1. The system of indexing SBs and CBs may be arbitrary, but some systems may render computations more effective.

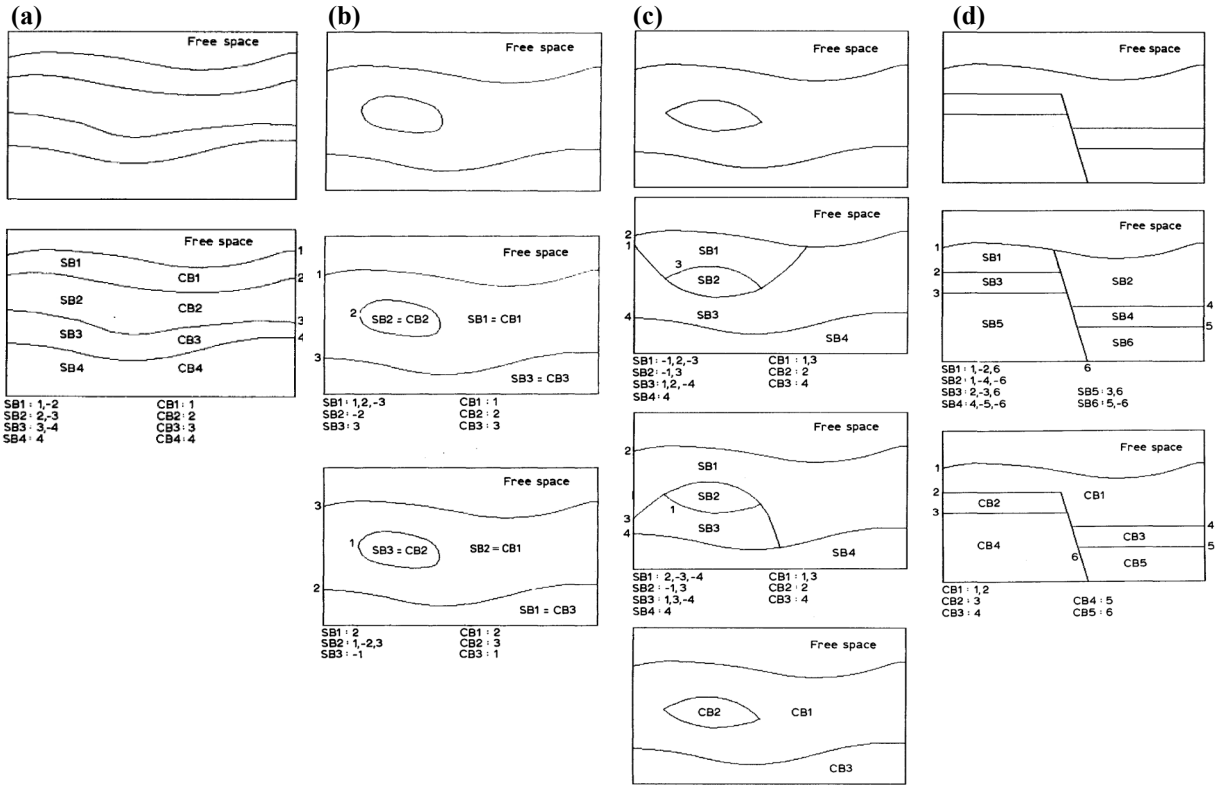


**Figure 15**. Four examples illustrating the method to describe 3D models in the CRT program. The figures are taken from Figure 3 – 6 in Červeny et al. [1988].

Some demo models presented in Červeny et al. [1988] are shown in Figure 15. Figure 15a shows a model with a simple layered structure. The layers are separated by non-intersecting smooth interfaces. Each layer is represented by one SB, and CBs are identical with the SBs. Figure 15b shows a layered structure model containing an isolated body. Two different systems of indexing surfaces and SBs are used to represent the model. For example, in the middle panel of Figure 15b, the top layer is indexed by 1, the bottom layer is indexed by 3, and the surface enclosing the isolated body is indexed by 2. Therefore, the SB1 is defined by the downward side (defined as positive) of surface 1, the upward side (defined as negative) of surface 3, and the

outward side (defined as positive) of surface 2. The SB2 is defined by the inward side (defined as negative) of surface 2. The SB3 is defined by the downward side of surface 3. The boundaries of SB1 and SB3 also contain parts of the boundaries of the model volume.

The model shown in Figure 15c looks like that in Figure 15b, but the construction method for SBs is different because the isolated body in Figure 15c has sharp (non-smooth) edges. Some auxiliary surfaces must be added by extending the actual surfaces of the block to form SBs. Two possible representations of the model in terms of SBs are shown in Figure 15c. In this example, although the region represented by SB1 and SB3 is one physical unit, it cannot be represented by one SB, but SB1 and SB3 may be united to form one CB of the same physical properties. CB2 and CB3 are identical to the SBs. Figure 15d shows a model of a simple fracture structure with a sedimentary cover. SB1 and SB2 may be united to form a CB, and the other CBs are identical to SBs. These demos show that the division of models into SBs may be non-unique and such division provides great flexibility to describe any complicated 3D model for various ray tracing simulations.

## 3.3 Demo CRT Calculation

We parameterized the model shown in Figure 15c and used it to perform a demo CRT calculation. The model space is set in a Cartesian coordinate system so that the covariant components, contravariant components, and Christoffel symbols are:

$$G_{ij} = \delta_{ij},\ G^{ij} = \delta^{ij},\ \text{and}\ \Gamma_{ij}^{k} = 0, \tag{6}$$

respectively. Surfaces 1 and 3 are intersecting 3D surfaces forming an isolated block in the model space (Figure 16). Surfaces 2 and 4 have only 2D structures, and their structures along axis Y are constant. We assigned different velocity and density values to the three CBs. Within each CB, the velocity and density were constant. In practice, we can use 1D or 3D physical parameters in a CB.

The direction of a seismic ray leaving a source point is described by azimuth and take-off angle. The CRT program has the capability of computing a group of rays by providing a range of azimuths and take-off angles. In this demo, we compute a group of rays leaving the source at [25.0, 5.0, -23.0] towards different directions (Figure 17). The azimuths are chosen from 20° to 270° with a step of 45°. Note that the azimuth in the program is measured from axis X or the east direction in geographic coordinates. It is different from the geographic definition for azimuth, which is measured from the north direction. The take-off angles are chosen from 0° to 80° with a step of 20°, corresponding to upward seismic rays. The take-off angle is measured from the horizontal. The downward rays can also be computed by assigning negative take-off angles.

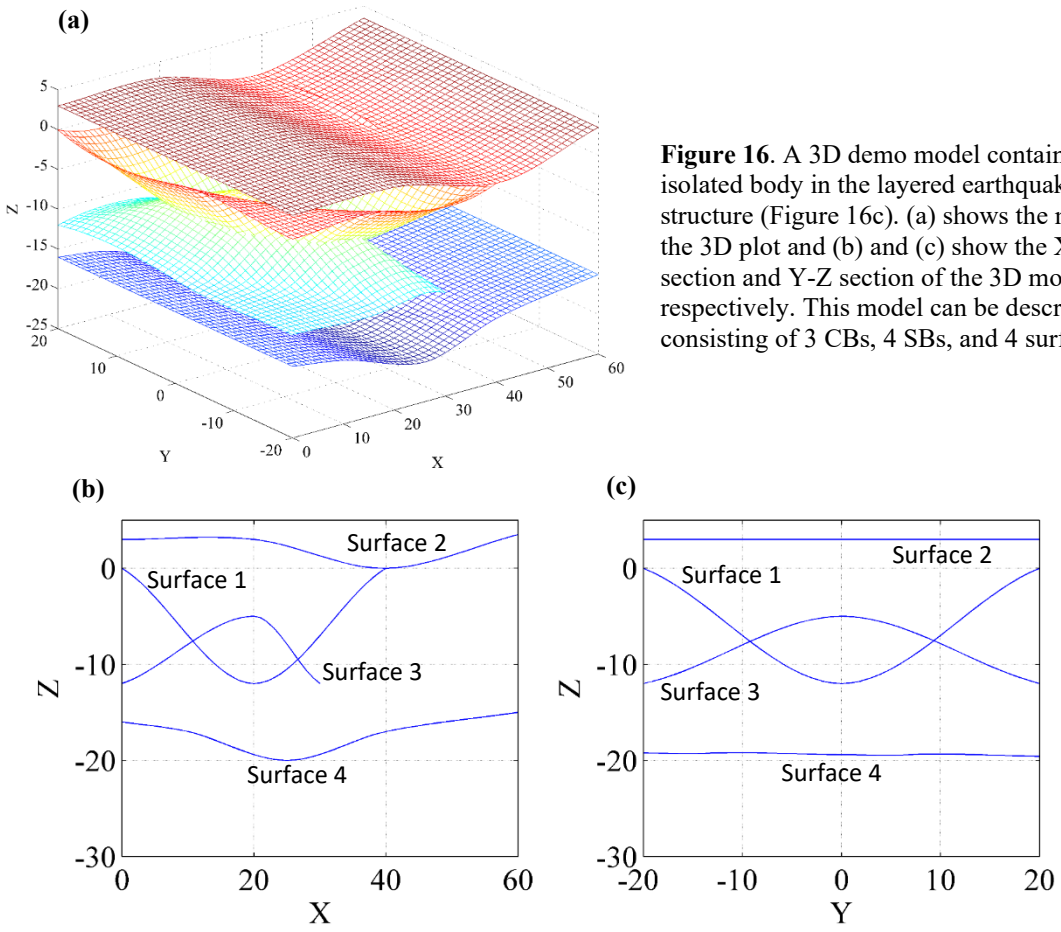


**Figure 16**. A 3D demo model containing an isolated body in the layered earthquake structure (Figure 16c). (a) shows the model in the 3D plot and (b) and (c) show the X-Z section and Y-Z section of the 3D model, respectively. This model can be described by consisting of 3 CBs, 4 SBs, and 4 surfaces.

Figure 17 shows the computed coordinates (blue dots) along each ray for P-wave, which are part of the output of the CRT program. To view the distribution of computed rays clearly, we plot the rays projected on X-Z, Y-Z, and X-Y sections, respectively. The coordinates of points along the ray are not always computed at the interfaces separating the blocks with different parameters. The quantities on these interfaces are output in another specified file. In the CRT program, there are many criteria to terminate the ray tracing computation, such as when a ray intersects any boundary of the model volume, overcritical transmission, S-wave in a liquid block, and zero amplitudes of reflected or converted waves. Therefore, the ray tracing computation of some rays may be early-terminated before the rays reach the receivers on the free surface.

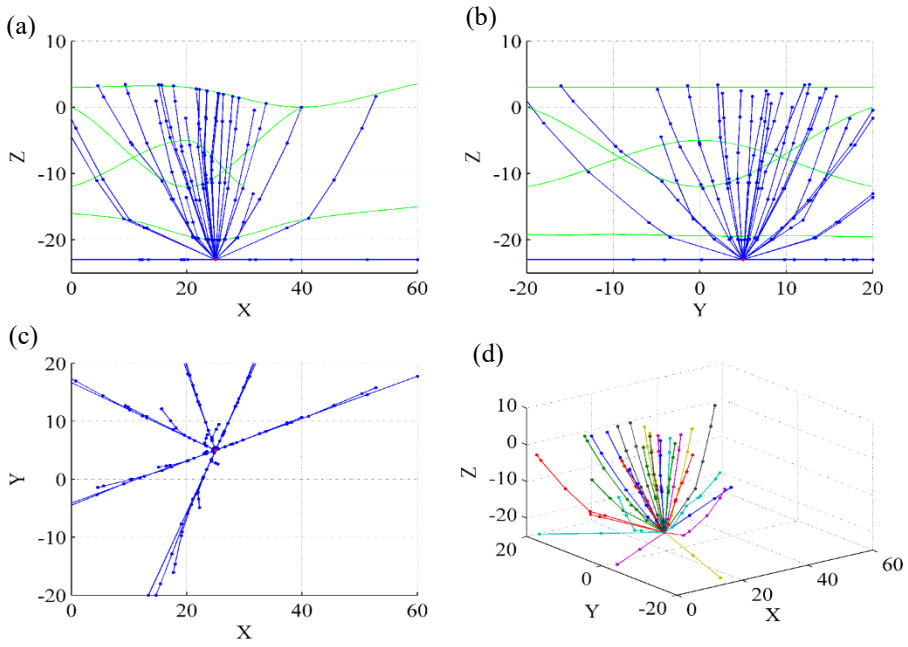


**Figure 17.** Computed seismic rays from a point source through the 3D model shown in Figure 13. The seismic rays leave the source with different azimuths and take-off angles. (a), (b) and (c) show the rays projecting on X-Z, Y-Z, and X-Y sections, respectively. (d) shows the rays in a 3D plot.

# 4 ANALYSES OF S-WAVE SHADOWS AND P-WAVE DELAYS

## 4.1 Classification of S-wave Shadows by S/P Ratios

The S-wave shadow means S-wave is missing on a seismogram and provides direct evidence for the molten or partially molten magma reservoir beneath a volcano. When the seismic wave encounters magma that is either molten or hot enough, the S-wave is prevented from passing through the magma. S-wave shadows can be easily detected by visual inspection as we observed in seismic phase picking. Figures 18 and 19 show more examples of S-wave shadows. The 3-component seismogram of earthquake 2010.02.21_07.29.083 (Table 1) recorded at three typical stations is plotted in Figure 18. This earthquake occurred on the boundary of China, North Korea, and Russia at a depth of 563km and was recorded by 74 stations. The seismograms recorded in NE China can be classified into three categories: (1) Clear S phase is observed on vertical, radial, and tangential components (e.g., YP.NE4B in Figure 18a). (2) S phase is observed only on two horizontal components but is weak on the vertical component (e.g., YP.NE4A in Figure 18b). (3) S amplitudes are attenuated on all three components (e.g., YP.NE12 in Figure 18c). In this example, station YP.NE12 is only about 100km from the CBS volcano.

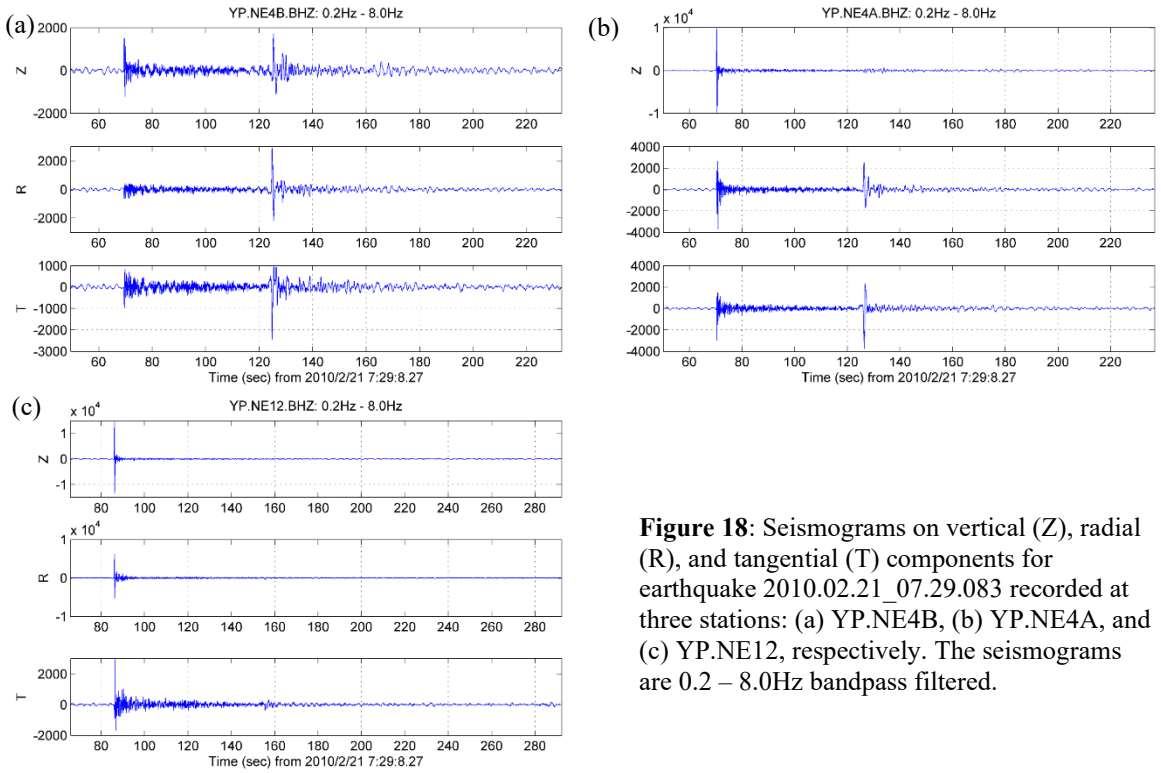


**Figure 18**: Seismograms on vertical (Z), radial (R), and tangential (T) components for earthquake 2010.02.21_07.29.083 recorded at three stations: (a) YP.NE4B, (b) YP.NE4A, and (c) YP.NE12, respectively. The seismograms are 0.2 – 8.0Hz bandpass filtered.

Figure 19 shows the three typical seismograms of another earthquake 2010.02.05_06.48.103. This earthquake occurred in the Sea of Japan at a depth of 370km (Table 1). At station YP.NE4B, clear S phase occurs on all three components (Figure 19a). At station YP.NE4A, clear S phase occurs only on horizontal components (Figure 19b). At station YP.NE12, the S phase is heavily attenuated on all three components (Figure 19c). However, it is interesting to note that station YP.NE12 is in the northwestern part of NE China, far away from active volcanic areas in NE China.

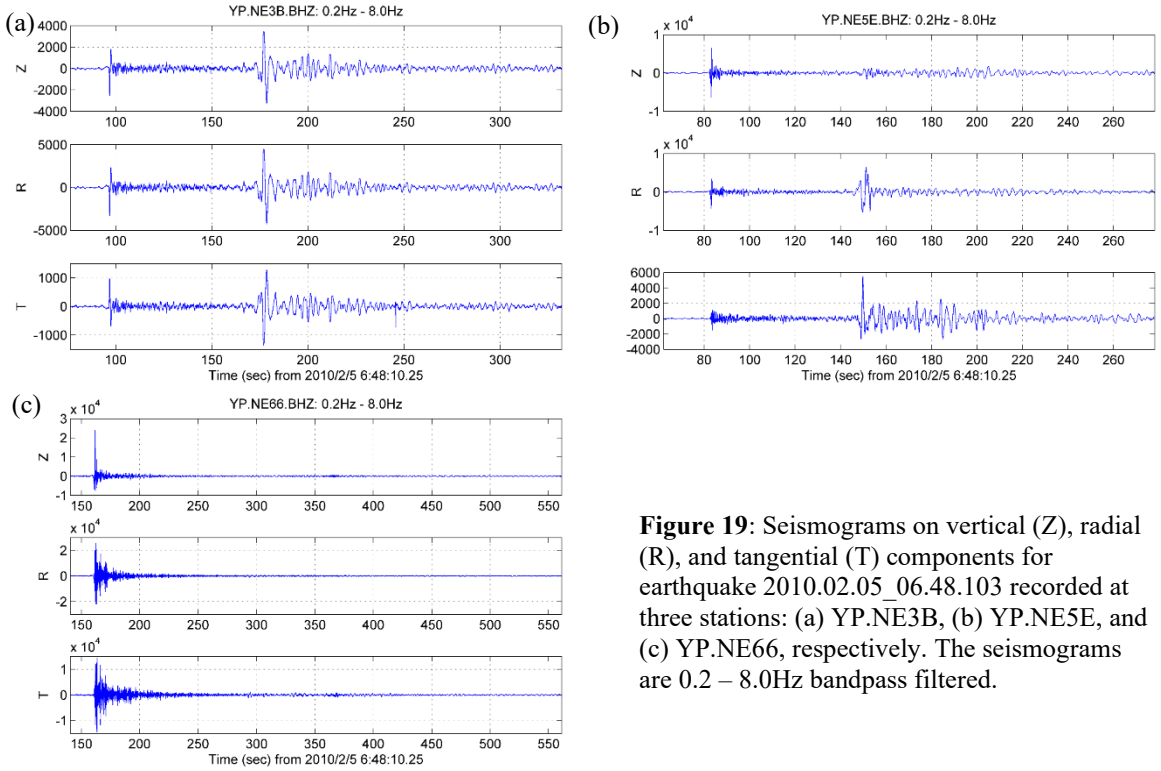


**Figure 19**: Seismograms on vertical (Z), radial (R), and tangential (T) components for earthquake 2010.02.05_06.48.103 recorded at three stations: (a) YP.NE3B, (b) YP.NE5E, and (c) YP.NE66, respectively. The seismograms are 0.2 – 8.0Hz bandpass filtered.

In addition to visual inspection, we calculated the S/P amplitude ratio on a seismogram to quantify the S-wave shadow. Using the picked P arrival as the starting point, we set a 5s window as the direct P wave duration. In the P wave window, we find the peak or trough of the P wave and calculate the RMS amplitude of the P wave by using the amplitudes of one period before the peak (or trough) and one period after the peak (or trough). Similarly, the S-wave duration is defined as a 10s window after the picked S arrival. If the S arrival is unidentifiable, the theoretical S arrival is used. The RMS amplitude of the S wave is calculated by using the amplitudes of one period before the S wave peak (or trough) and one period after the peak (or trough). The S/P amplitude ratio is then calculated using the RMS amplitudes of the S and P waves. Since the energy of the S-wave is mainly concentrated on horizontal components, we calculated the S/P ratio on the radial (R) and tangential (T) components individually and on both horizontal (H) components.

Figure 20 shows the geographic distribution of the stations (triangles in Figure 20) with S/P amplitude ratios calculated for event 2010.02.21_07.29.083. The values of S/P ratios are represented by the colors of triangles, with red for the minimum S/P value and blue for the maximum S/P value. The distributions of S/P amplitude ratios calculated using different horizontal components (R, T, and H) are consistent. For this earthquake, stations with extremely low S/P ratios (red triangles in Figure 20) are mainly concentrated north of the CBS volcano. Station YP.NE12 is a representative of the stations with extremely low S/P ratios. Similarly, Figure 21 shows the distribution of S/P amplitude ratios for another event 2010.02.05_06.48.103. Interestingly, however, we found that most of the stations with extremely low S/P ratios for this earthquake are concentrated in the northwestern part of NE China, far away from the active volcanic areas in NE China.

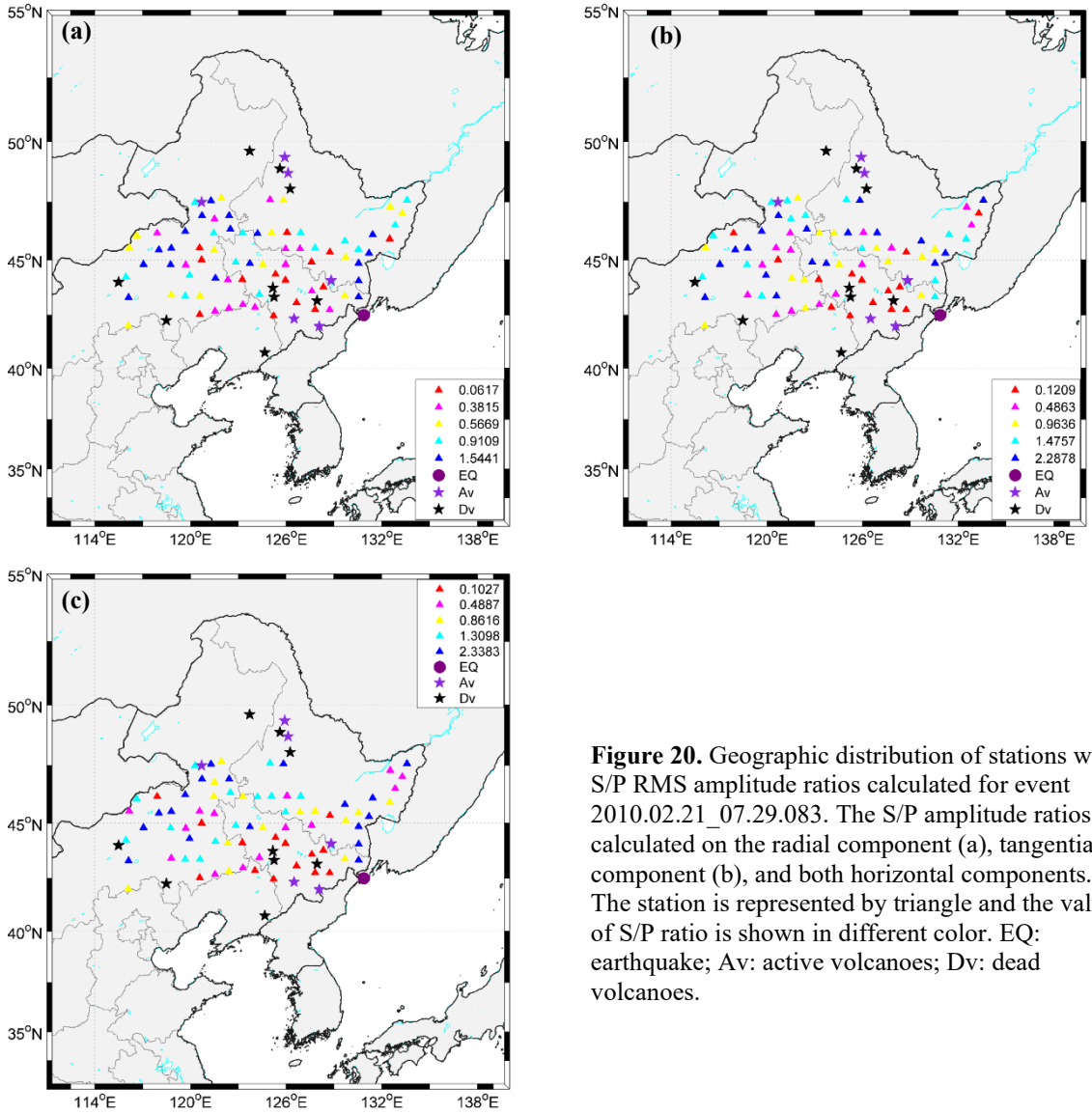


**Figure 20.** Geographic distribution of stations with S/P RMS amplitude ratios calculated for event 2010.02.21_07.29.083. The S/P amplitude ratios are calculated on the radial component (a), tangential component (b), and both horizontal components. The station is represented by triangle and the value of S/P ratio is shown in different color. EQ: earthquake; Av: active volcanoes; Dv: dead volcanoes.

These two earthquakes have different depths and epicentral distances to NE China stations. The seismic waves leaving two sources thus scan different parts of the upper mantle and crust beneath NE China. Event 2010.02.21_07.29.083 is located right below the CBS volcano at a depth of 563km. Suppose molten magma exists below the CBS volcano. In that case, the S-wave shadow phenomenon will positively correlate with the spatial distribution of the stations receiving seismic waves: the stations showing S-wave shadows should be near the CBS volcanic region. At the same time, clear S-waves are observed at stations far from the volcano (Figure 20). On the other hand, event 2010.02.05_06.48.103 occurred southeast of the CBS volcano at about 1000km and a depth of 370km. The seismic rays of this earthquake propagate northwestward to the stations in NE China and show significant S-wave shadows at the stations in this direction. These seismic rays do not pass through the crust below the CBS volcano, but rather through portions of the upper mantle that are also scanned by the seismic rays of event 2010.02.21_07.29.083. It suggests the presence of molten magma somewhere in the upper mantle below the CBS volcano. However, we

may not rule out the probability of small molten magma in the crust below the stations showing S-wave shadows.

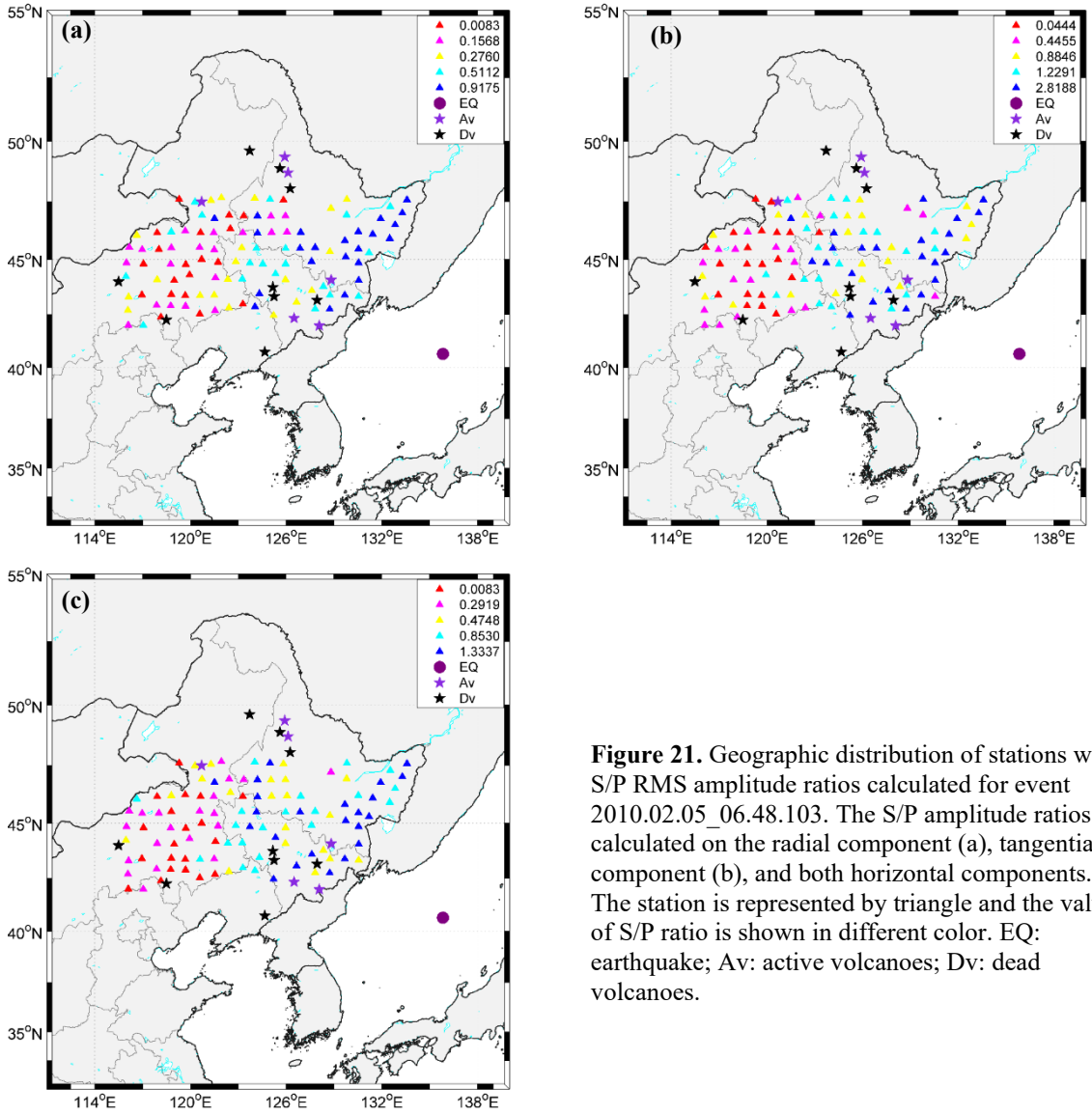


**Figure 21.** Geographic distribution of stations with S/P RMS amplitude ratios calculated for event 2010.02.05_06.48.103. The S/P amplitude ratios are calculated on the radial component (a), tangential component (b), and both horizontal components. The station is represented by triangle and the value of S/P ratio is shown in different color. EQ: earthquake; Av: active volcanoes; Dv: dead volcanoes.

In Section 5, we will perform ray tracing simulations for all deep earthquakes. The seismic rays of these earthquakes scan different portions of the crust and upper mantle below the CBS volcano. The distribution of seismic rays showing S-wave shadows in 3D space allows us to delimit the size and depth of the potential magma reservoir.

## 4.2 Observation of P-wave Delays

We observed P-wave delays when manually picking seismic phases (Figures 13 and 14). In this section, we presented and analyzed P-wave delays using several example earthquakes. The first example is the earthquake 2010.02.18_01.13.184 (Table 1). Figure 22a shows the vertical-component seismograms of this earthquake recorded at the stations along the path across the CBS volcanic region. Figure 22b shows the surface projection of seismic rays propagating along this path. The theoretical P and S arrivals are calculated using the AK135 global velocity model and

are plotted in green and magenta curves in Figure 22a, respectively. It shows that the actual P arrivals to all stations on this path are delayed compared to the theoretical arrivals. The S arrivals are also delayed compared to the corresponding theoretical arrivals; however, a closer inspection of the seismograms reveals that the S-wave shadows do not completely coincide with the P-wave delays. On all components, weak or missed S-waves are only found at stations near the CBS volcano, such as JL.SMT, JL.CBS, JL.MJT, JL.YFT, JL.THT, and LN.HUR, while on the stations more than ~500km away from the volcano, the S-waves have relatively strong amplitudes. The Longgang volcano is only ~136km west of the CBS volcano (Figure 1). P-wave delays and S-wave shadows are also observed at the stations around the Longgang volcanic region.

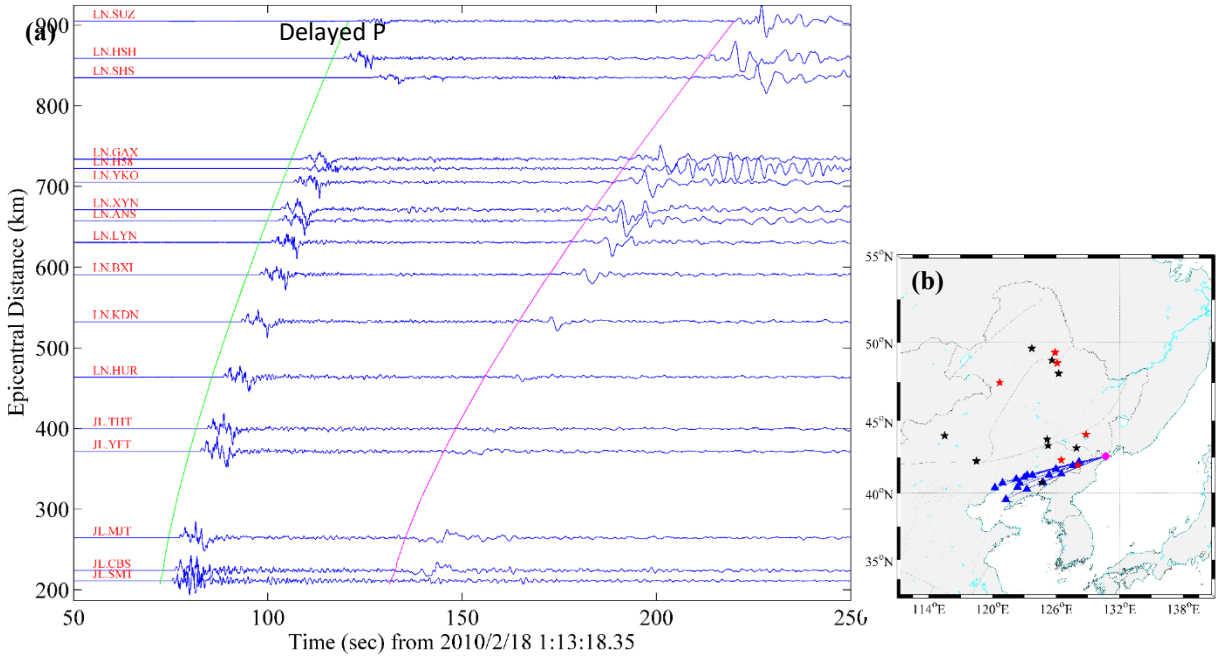


**Figure 22.** The vertical-component seismograms of earthquake 2010.02.18_01.13.184 recorded at the stations on the path crossing through the CBS volcanic region. The seismograms are sorted in epicentral distances. The green and magenta curves denote predicted P and S arrivals, respectively. (b) Map showing the surface projection of seismic rays propagating along the path across CBS. Red stars stand for active volcanoes and black starts stand for dead volcanoes.

Figure 23 shows the geographic distribution of S/P amplitude ratios calculated on the tangential component seismograms. The spatial variation pattern of S/P ratios shows a rough correlation with the distances to the CBS volcanic regions: the S/P ratios with low values (red and magenta triangles) are concentrated in an area surrounding CBS and Longgang volcanos.

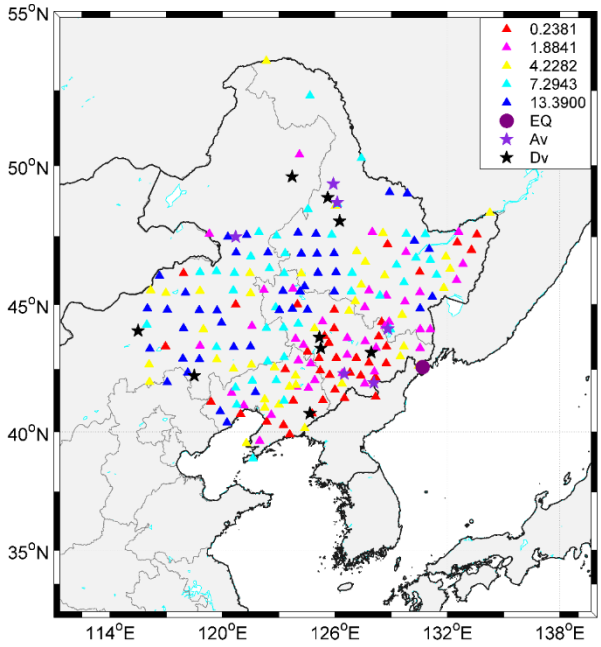


**Figure 23.** Geographic distribution of stations with S/P RMS amplitude ratios calculated for event 2010.02.18_01.13.184. The S/P amplitude ratios are calculated on the tangential component. The station is represented by triangle and the value of S/P ratio is shown in different color. EQ: earthquake; Av: active volcanoes; Dv: dead volcanoes.

Figure 24 shows the vertical-component seismograms of the second representative earthquake 2011.01.07_23.34.106 (Table 1) recorded at the stations along the path across the CBS volcanic region. Figure 25 shows the vertical-component seismograms of this earthquake recorded at the stations along a path deviating away from any active volcanic areas in NE China. Comparing the P-wave arrivals along the two paths, we do not find significant P-wave delays along the path far from any active volcanic area, but short P-wave delays can be observed for the path passing through the CBS volcanic area. For this earthquake, the S-wave amplitudes on the vertical components are generally weak or missing, including some seismograms recorded at stations far from volcanic areas. On horizontal components, however, S-wave missing occurs only at the stations around volcanic areas, which can also be seen from the geographic distribution of the S/P amplitude ratios. Figure 26 shows the geographic distribution of the S/P amplitude ratios calculated on the tangential component. The stations with low S/P ratios (red and magenta triangles) are mainly concentrated around the CBS, Longgang, and Jingbo volcanoes.

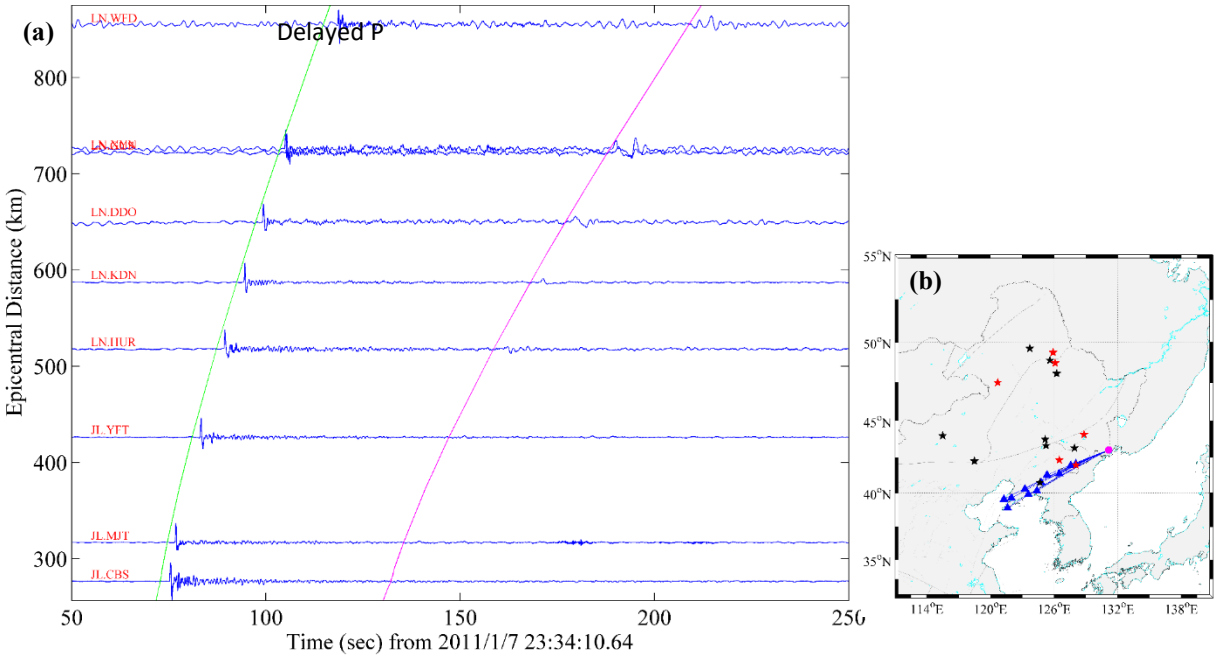


**Figure 24.** The vertical-component seismograms of earthquake 2011.01.07_23.34.106 recorded at the stations on the path crossing through the CBS volcanic region. The seismograms are sorted in epicentral distances. The green and magenta curves denote predicted P and S arrivals, respectively. (b) Map showing the surface projection of seismic rays propagating along the path across CBS. Red stars stand for active volcanoes and black starts stand for dead volcanoes.

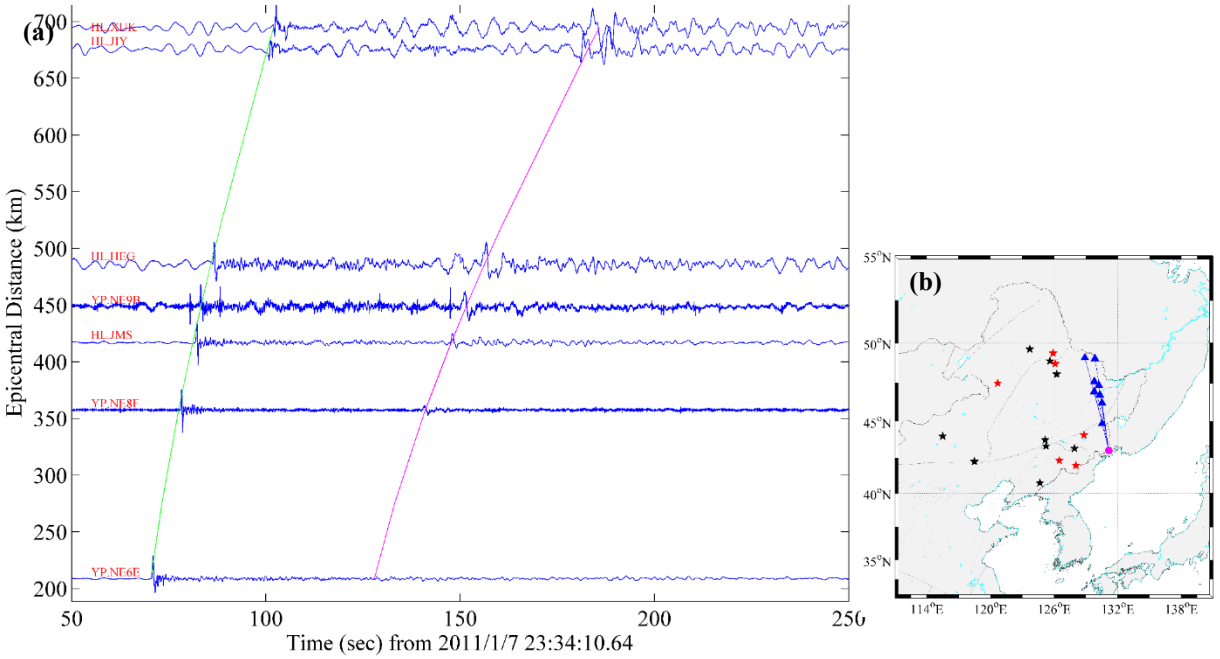


**Figure 25.** Same as Figure 24, but for the seismograms recorded at the stations on the path far away from any active volcanic areas in NE China.

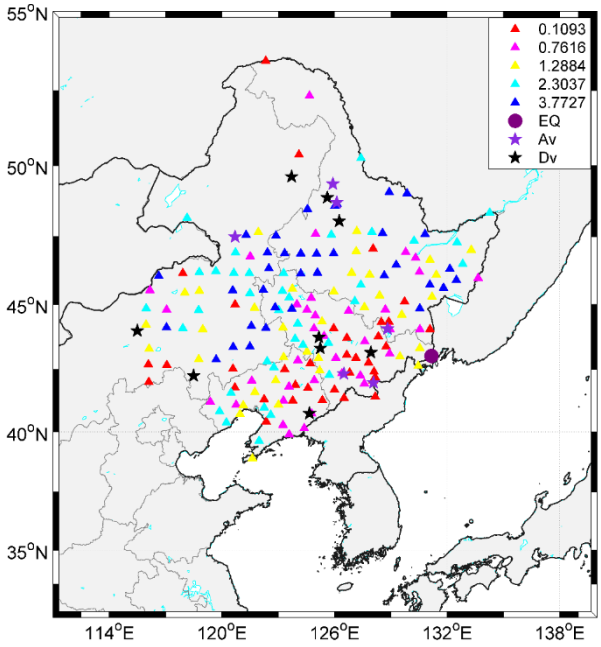


**Figure 26.** Geographic distribution of stations with S/P RMS amplitude ratios calculated for event 2011.01.07_23.34.106. The S/P amplitude ratios are calculated on the tangential component. The station is represented by triangle and the value of S/P ratio is shown in different color. EQ: earthquake; Av: active volcanoes; Dv: dead volcanoes.

The last representative earthquake we present here is 2015.11.07_13.44.445 (Table 1). This earthquake has a much shallower focal depth (109km) than the first two representative earthquakes and is more than 1000km away from the stations in NE China. The original seismograms of this earthquake are noisy, and we filtered the original seismograms using a bandpass filter with corner frequencies of 0.1 and 8.0Hz. Figure 27 shows the vertical-component seismograms recorded at the stations along the paths across the CBS volcano. A close look reveals short P-wave delays in seismograms along this path. Because the Longgang volcano is in the same direction as this earthquake propagating to the CBS volcano (Figure 27b), we cannot judge whether there is a magma reservoir under the Longgang volcano. At most stations, the vertical S-wave amplitudes are also very weak, but they can be identified in the horizontal components. The geographic distribution of the S/P amplitude ratios calculated on the tangential component (Figure 28) shows that the stations with low S/P ratios (red and magenta triangles) are mainly concentrated around the CBS and Longgang volcanoes. There are also several stations around the CBS and Longgang volcanoes showing high S/P ratios. It probably means that the S-wave shadows are caused by local, small-size molten magma in the crust or uppermost mantle.

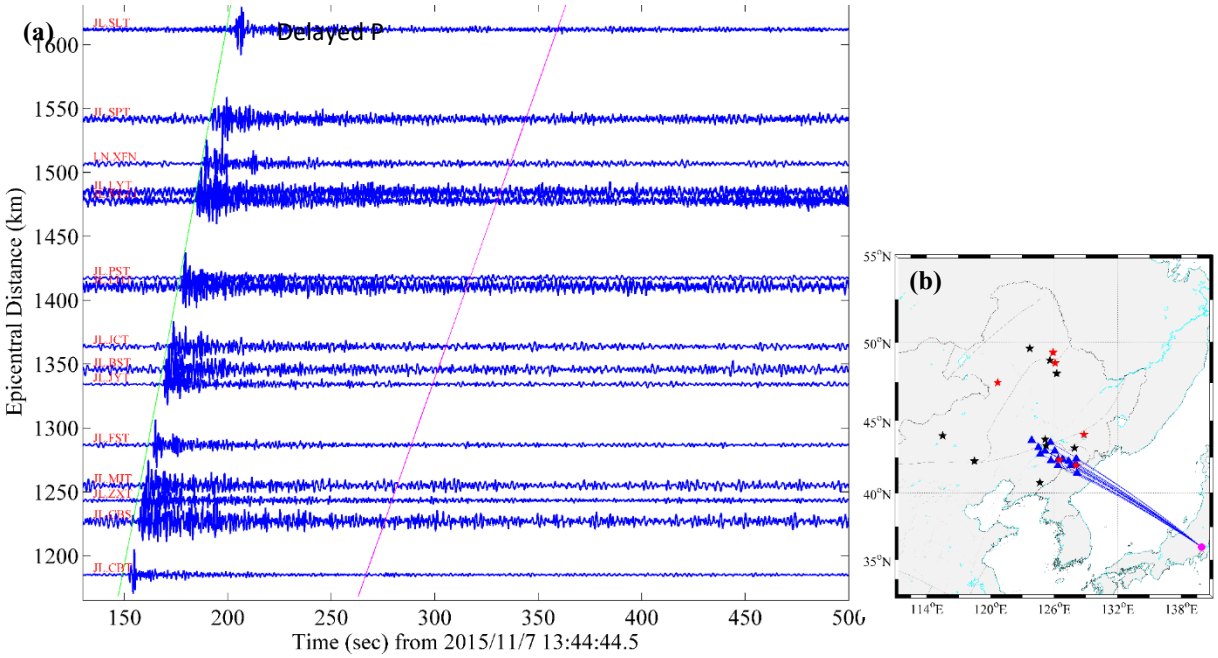


**Figure 27.** The vertical-component seismograms of earthquake 2015.11.07_13.44.445 recorded at the stations on the path crossing through the CBS volcanic region. The seismograms are sorted in epicentral distances. The green and magenta curves denote predicted P and S arrivals, respectively. (b) Map showing the surface projection of seismic rays propagating along the path across CBS. Red stars stand for active volcanoes and black starts stand for dead volcanoes.

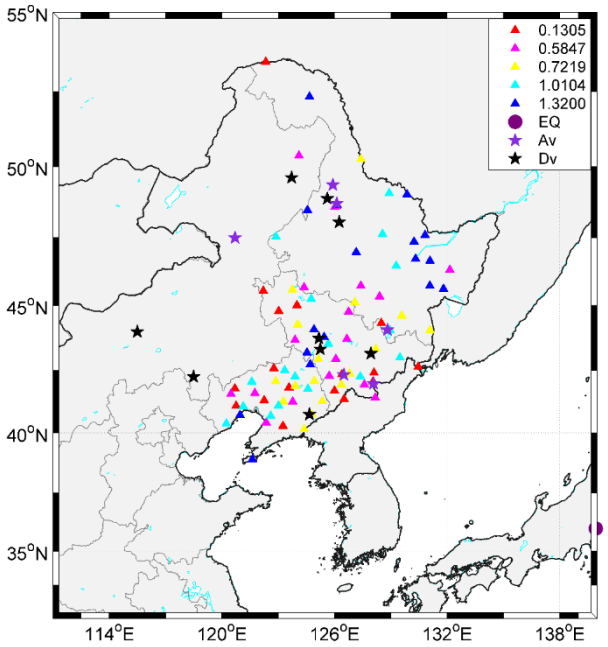


**Figure 28.** Geographic distribution of stations with S/P RMS amplitude ratios calculated for event 2015.11.07_13.44.445. The S/P amplitude ratios are calculated on the tangential component. The station is represented by triangle and the value of S/P ratio is shown in different color. EQ: earthquake; Av: active volcanoes; Dv: dead volcanoes.

# 5 SEISMIC RAY TRACING SIMULATIONS

## 5.1 Construction of a Layered Model

We built a layered model to perform seismic ray tracing simulations for our problem. According to the results of previous studies, we set the spatial range of the model as 33.5° - 48.5° in latitude, 115.5° - 140.5° in longitude, and 700km in depth. All the stations and earthquakes used in this study are contained in this model space (Figure 10 and Figure 11). The maximum depth of the model extends to 700km as there are no deep earthquakes beyond 700km (Figure 10 and Table 1). Farther areas are unaffected by the CBS magma reservoir.

The layered model is based on the 1D AK135 velocity model (Figure 12). In the 1D AK135 model, the crust consists of two layers with uniform P and S velocities. The Moho discontinuity is located at 35km. The upper mantle discontinuities are at 410km and 660km, respectively. Between the mantle discontinuities, the velocities have a gradient structure. We modified the AK135 model to add 3D topography for the free surface and the Moho interface. In our model space, the ETOPO1 global relief model [https://www.ngdc.noaa.gov/mgg/global/] was used to replace the free surface. The Moho was replaced with the 3D Moho relief model obtained by Chen and Niu [2016]. The crustal and upper mantle parts of the model we constructed are shown in Figure 29.

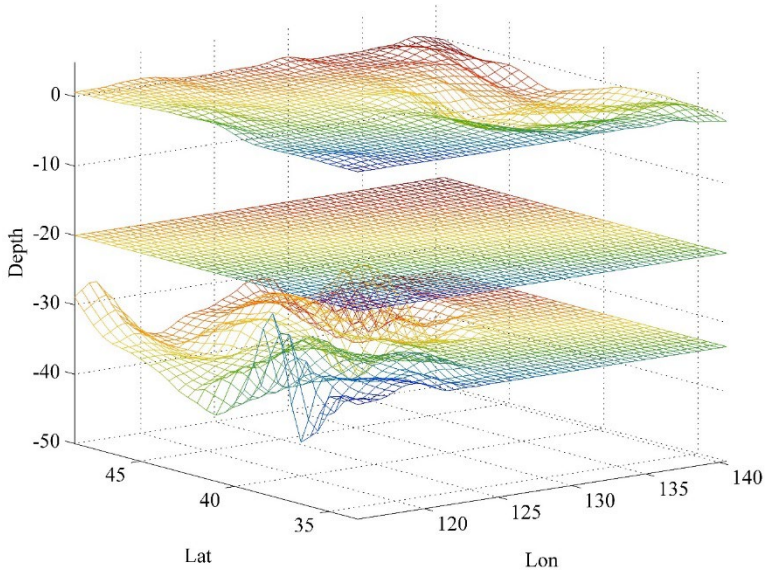


**Figure 29.** .3D plot of the crust and upper mantle parts of the model for ray tracing calculation. The rest parts of the model are taken from the AK135 model. Our model extends to 700km deep and uses geographic coordinates.

We used a geographic spherical coordinate system for our model, so the metric tensor is:

$$G_{ij} = \begin{bmatrix} r^2 cos^2\theta & 0 & 0 \\ 0 & r^2 & 0 \\ 0 & 0 & 1 \end{bmatrix}, G^{ij} = \begin{bmatrix} r^{-2} cos^{-2}\theta & 0 & 0 \\ 0 & r^{-2} & 0 \\ 0 & 0 & 1 \end{bmatrix}, \quad (7)$$

respectively, and the Christoffel symbols are

$$\Gamma^1_{ij} = \begin{bmatrix} 0 & -tan\theta & r^{-1} \\ -tan\theta & 0 & 0 \\ r^{-1} & 0 & 0 \end{bmatrix}, \Gamma^2_{ij} = \begin{bmatrix} sin\theta\, cos\theta & 0 & 0 \\ 0 & 0 & r^{-1} \\ 0 & r^{-1} & 0 \end{bmatrix}, \Gamma^3_{ij} = \begin{bmatrix} -r cos^2\theta & 0 & 0 \\ 0 & -r & 0 \\ 0 & 0 & 0 \end{bmatrix}, \quad (8)$$

where $\theta$ is the latitude and $r$ is the radial distance.

Because the CRT is a forward ray-tracing program, it can compute multiple seismic rays leaving a source with prescribed azimuths and take-off angles but cannot determine a ray with the prescribed source and receiver. We first compute a group of seismic rays by setting a range of azimuths and take-off angles, then gradually adjust the azimuths and take-off angles until the ray reaches the desired receiving site [Chen, 1998]. We only calculate seismic rays to the stations with available seismic data.

## 5.2 Results of Seismic Ray Tracing

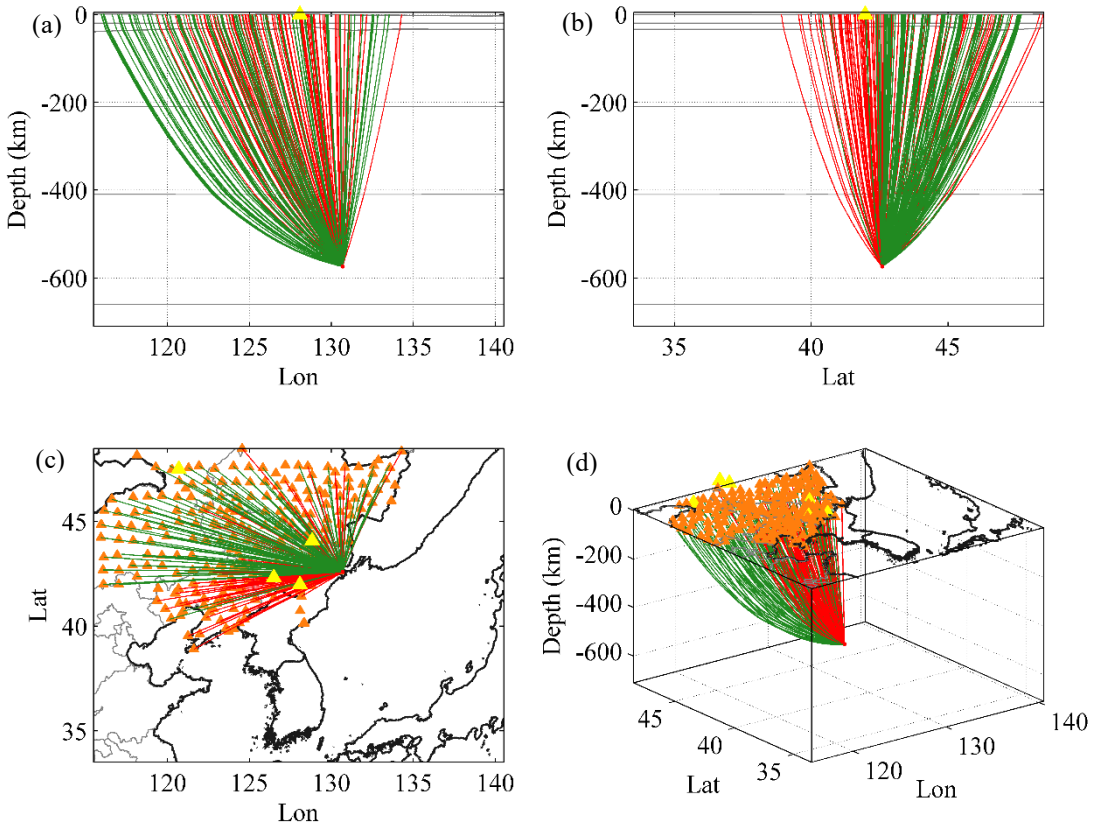


**Figure 30.** The synthetic ray tracing results for the earthquake 2010.02.18_01.13.184. The ray tracings are calculated only for the stations with seismic data. (a) The seismic rays projecting on the section at the longitude across the CBS volcano. (b) The seismic rays projecting on the section at the latitude across the CBS volcano. (c) All seismic rays projecting on the surface. (d) All seismic rays in a 3D view. The orange triangles stand for seismic stations and the yellow triangles stand for active volcanoes. The red seismic rays indicate that they have significant P-wave delays with travel time residue ≥ 3.0s.

We present the results of ray tracing simulations by using several representative earthquakes. The first example is event 2010.02.18_01.13.184, which was used in Section 4.2 to demonstrate P-wave delays. The calculated seismic rays using our layered model are shown in Figure 30. As this earthquake is right below the CBS volcano at a depth of 574km, its seismic rays almost vertically propagate through the entire upper mantle and crust to the stations in NE China. For each station with usable seismic data, a travel time residue is defined as the picked P-wave time minus the predicted time calculated by the CRT program. In Figure 30, the seismic rays with significant P-wave delays (i.e., travel time residues ≥ 3.0s) are plotted in red. The spatial distribution of such seismic rays indicates that the P-wave delays are related to the underlying magma reservoirs beneath the CBS and Longgang volcanoes, consistent with the P-wave delays

observed from the seismograms (Figure 22) and the S-wave shadows observed from the distribution of S/P ratios (Figure 23). The potential magma reservoir could be located at any depth in the upper mantle and crust along the seismic ray paths.

The second representative earthquake is 2010.02.05_06.48.103, and the ray tracing simulation results are shown in Figure 31. This event occurred in the southeast of the CBS volcano at about 1000km and a depth of 370km, so its seismic rays scan the upper mantle and crust at shallower incidence angles than the seismic rays of the first representative event. Many stations far from the CBS volcano show prominent S-wave shadows (Figure 21), but they do not show significant P-wave delays (Figure 31). As shown in Figure 31, only a few seismic rays have travel time residues ≥ 2.0s (red rays in Figure 31), and they are captured by stations far from the CBS volcano. It implies that no matter where it is located, the molten magma has a small scale, so it blocks the propagation of S-waves but does not cause significant P-wave delays.

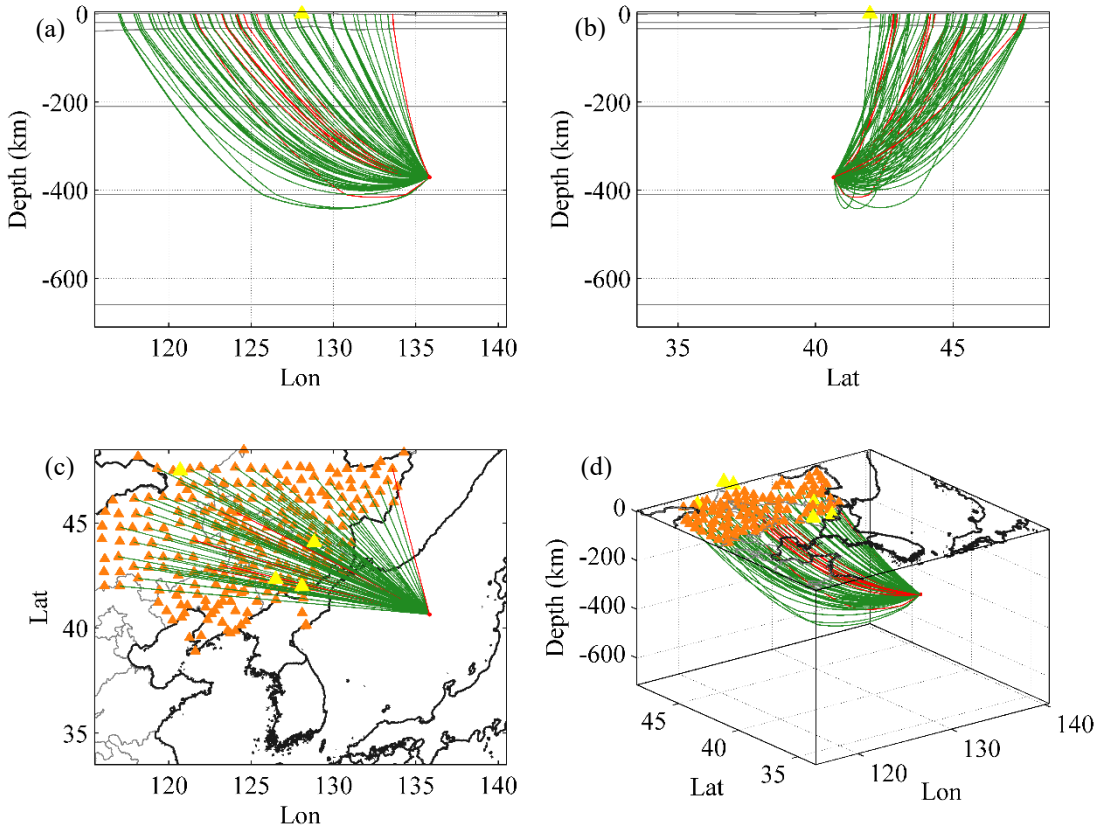


**Figure 31.** Same as Figure 30, but for earthquake 2010.02.05_06.48.103. The red seismic rays indicate that they have significant P-wave delays with travel time residue ≥ 2.0s.

The last representative earthquake, 2015.11.07_13.44.445 (Table 1), occurred in the Sea of Japan. Of the three representative earthquakes presented here, it has the shallowest depth at 109km. The ray tracing simulation for this earthquake Figure 32) shows that seismic rays mainly propagate in the upper mantle and crust within 300km. As a result, the ray paths of this earthquake are more complex than those of the other two representative earthquakes. The seismic rays with significant P-wave delays (travel time residues ⩾ 2.0s) are limited to the top 150km and are related to the magma reservoir below the CBS and Longgang volcanoes. S-wave shadows are also observed at the stations around the CBS and Longgang volcanoes (Figure 28). Our results indicate that the

potential magma reservoir is constrained in the uppermost mantle and crust below the CBS volcano.

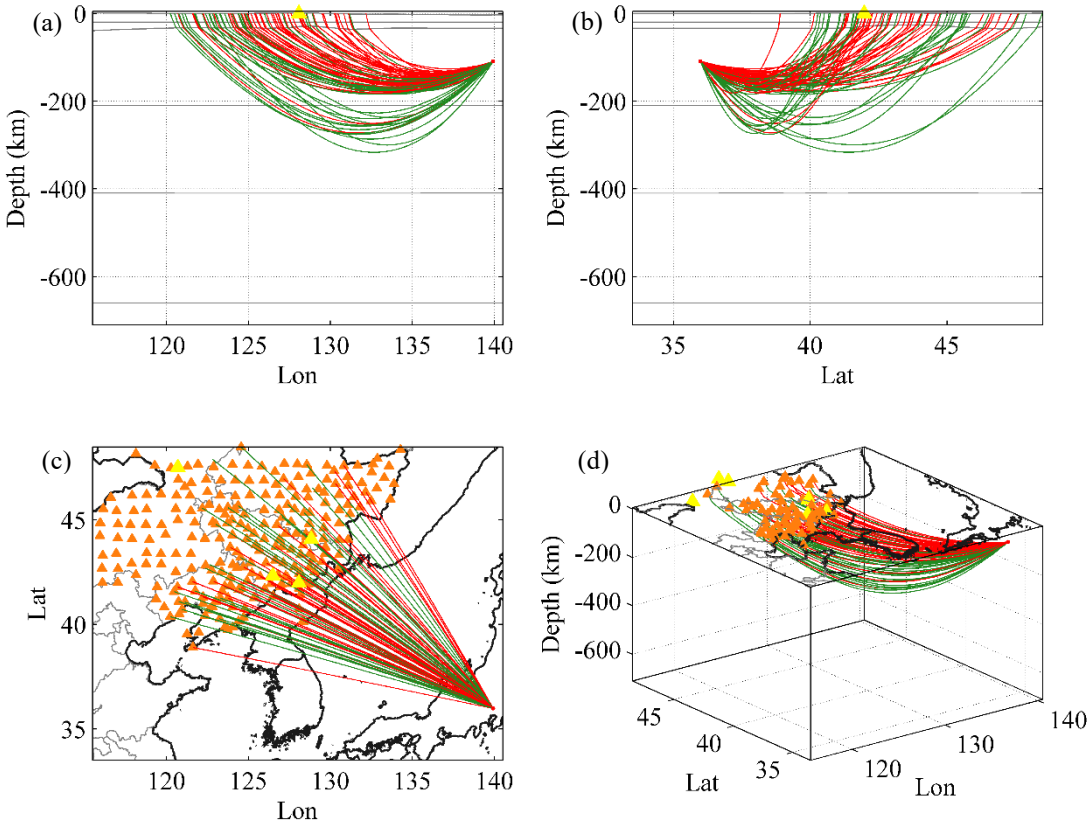


**Figure 32.** Same as Figure 30, but for earthquake 2015.11.07_13.44.445. The red seismic rays indicate that they have significant P-wave delays with travel time residue ≥ 2.0s.

## 5.3 Melton Magma and Low-Velocity Zone

We performed ray-tracing simulations for all earthquakes using the layered model. For each seismic ray of an event, the spatial position and travel time of the travel path from the source to the recording station were calculated. We picked out the seismic rays with significant S-wave shadows and P-wave delays, respectively. Seismic rays with an S/P amplitude ratio of less than 0.2 on the tangential or horizontal components are considered severely S-wave attenuated. We then visually inspected the seismograms of those seismic rays to ensure complete S-wave attenuation, as shown in Figures 18c and 19c. The spatial distribution of all seismic rays with S-wave shadows is plotted in Figure 33. The seismic rays are produced by different sources and recorded at different stations. Figure 33a shows these seismic rays in 3D view, and Figures 33b – 33d show the intersection points of these seismic rays at depths of 40, 200, and 400km, respectively. Similarly, we picked out the seismic rays with travel time residues ≥ 4.0s, and their spatial distribution is shown in Figure 34.

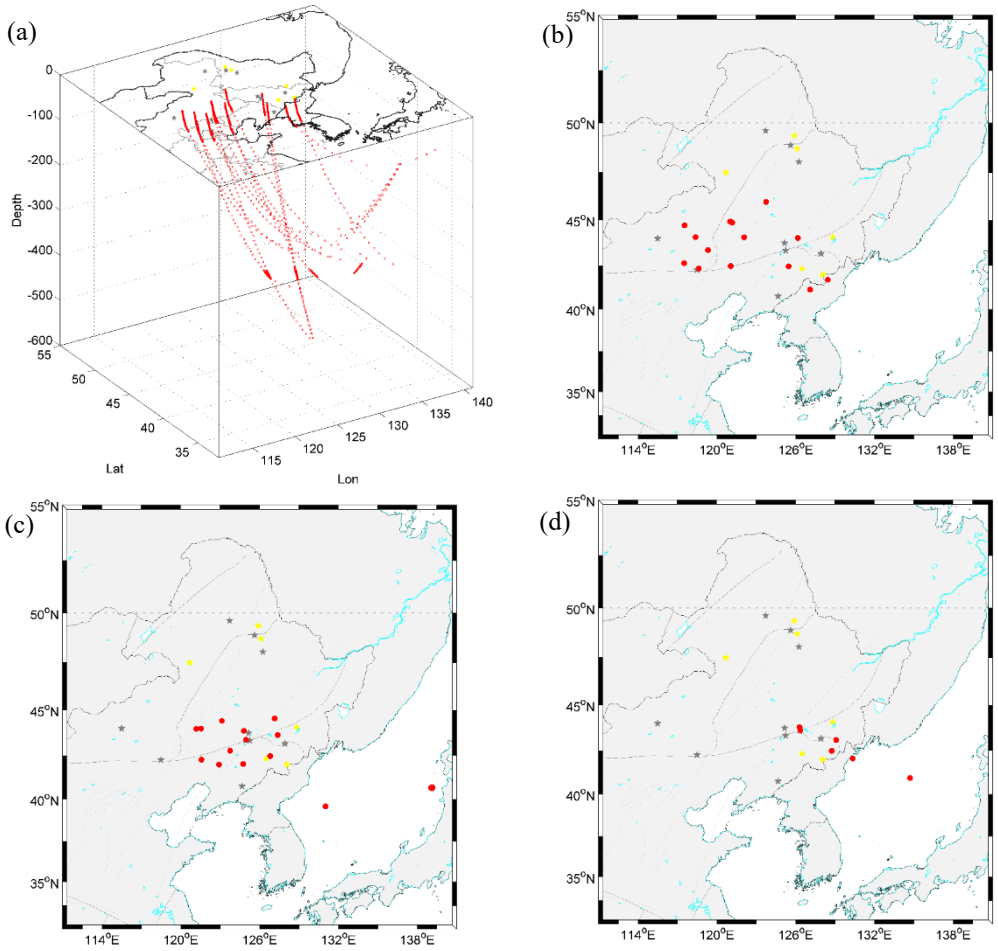


**Figure 33.** The ray tracing results for the seismic rays with S/P amplitude ratios less than 0.2 on the tangential component. (a) Spatial positions of such seismic rays in a 3D view. (b)-(d) The intersection points of seismic rays at a depth of 40km, 200km, and 400km, respectively.

Comparing Figure 33 to Figure 34, we can find that the spatial distribution of seismic rays with S-wave shadows does not coincide with that of the seismic rays with P-wave delays. Some stations showing significant S-wave shadows do not show large differences in P-wave delays and vice versa. The seismic rays with S-wave shadows exhibit a trend from northwest to southeast in NE China, and CBS is located at the southeast end. In contrast, the seismic rays with P-wave delays show a northeast-to-southwest trend through the CBS volcano, roughly along the CBS mountains. It may simply indicate that the large low-velocity zone exists in the crust and upper mantle, but the molten magma is restricted to small regions in the crust or upper mantle. The molten regions may appear as a thin lava layer overlying thick partially molten rock or many molten sills in partially molten rocks, as inferred by Lin [2016] for the Tatun volcano group of northern Taiwan. A small melt can prevent S-wave propagation but not enough to cause large P-wave travel time delays.

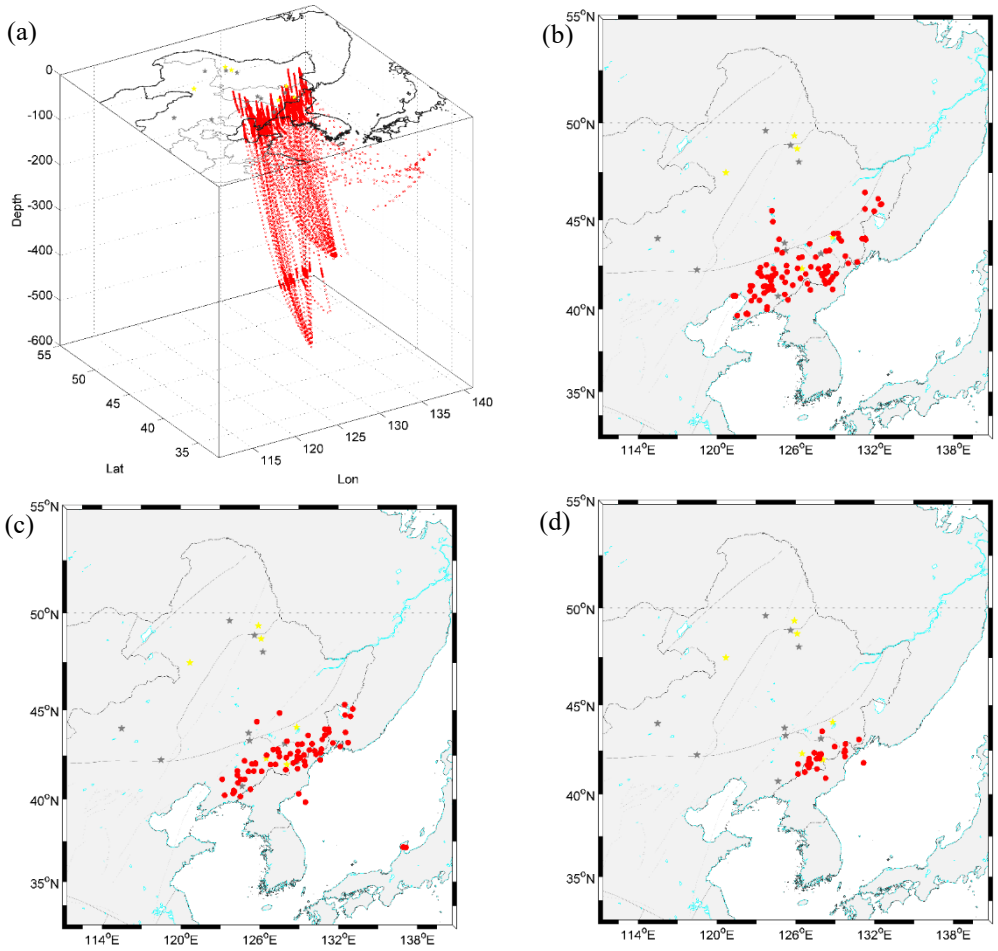


**Figure 34.** The ray tracing results for the seismic rays with travel time residues ≥ 4.0s. (a) Spatial positions of such seismic rays in a 3D view. (b)-(d) The intersection points of seismic rays at a depth of 40km, 200km, and 400km, respectively.

We speculated that the molten magma might exist in the upper mantle or the crust, but we currently do not have enough information to determine the depth. As shown in Figure 33, most seismic rays with S-wave shadows are produced by earthquakes at depths greater than 350km. These seismic rays overlap between 300 and 350km, suggesting a molten mass at this depth. For the earthquakes like 2010.02.05_06.48.103, which is about 1000km away from CBS and has a focal depth of 370km, the molten mass between 300 and 350km can cause S-wave shadows to be observed at the stations far away from the CBS volcanic area (Figure 21). On the other hand, we also noticed that some shallower earthquakes at depths of 100 – 200km produced S-wave shadows at stations near the CBS volcano, such as event 2015.11.07_13.44.445 (Figure 28). The seismic rays of these earthquakes never reach a depth of 300 – 350km (Figure 32). Combined with the acknowledged high crustal Vp/Vs ratio and low crustal velocity, it indicates the existence of molten magma in the crust.

# 6 DISCUSSION AND FUTURE WORK

The P-wave delays can be caused by a low-velocity zone through which seismic rays propagate, while S-wave shadows (attenuation) require the melt or partial melt of a media such as Earth's liquid outer core or subterranean magma reservoirs. Although some stations show both S-

wave shadows and P-wave delays, it is worth noting that most stations record only P-wave delays or only S-wave shadows, and there are more stations showing P-wave delays than S-wave shadow stations (Figures 33 and 34). Small-sized melts can severely attenuate or even block S-waves without significantly delaying the propagation of P-waves. On the other hand, the molten or partially molten media can induce large-scale low-velocity anomalies that further cause significant P-wave delays of many seismic rays.

Many tomographic models of NE China and the CBS region revealed low-velocity zones in the crust and upper mantle of the CBS Mountains [e.g., Lei and Zhao, 2005; Huang and Zhao, 2006; Tang et al., 2014; Zhu et al., 2019]. The low-velocity zone may extend to ~400km and span ~200km laterally with a cylindrical shape below CBS (Figures 3-5). Zhu et al. [2019] revealed a low-velocity body at depths of 8 – 15 km directly beneath the CBS volcano with a lateral extent of ~100 km in the north-south direction, which may reflect a large magma reservoir in the mid-crust (Figure 8). In our ray tracing simulations, seismic rays with significant P-wave delays are confined to the low-velocity region revealed by seismic tomography. Since many of the earthquakes in our study have focal depths over 400km, the seismic rays with significant P-wave delays at a depth of 400km are limited to an area approximately 200 to 400km directly below the CBS volcano. At shallower depths, seismic rays spread over a larger area as they travel to the surface (Figure 34). At a depth of 40km, the seismic rays expand to cover the entire CBS Mountains, but it does not mean that there are low-velocity zones everywhere below the CBS Mountains. If P-wave velocity is reduced by ~4% relative to the surrounding area, a low-velocity zone extending to ~400km is sufficient to cause a P-wave delay of ~4s for a deep earthquake recorded by the seismic stations in NE China. Complex Moho depth variations, inaccurate earthquake locations and depths, and local crustal velocity variations can all cause actual travel times to differ from theoretical travel times based on 1D velocity models. A more realistic local Earth model might reduce time residues, but it is difficult to believe that these factors would cause such significant travel time delays.

The receiver function, surface waves, or seismic noise interferometry data [e.g., Hetland et al., 2004; Ri et al., 2016; Kim et al., 2017; Hammond et al., 2019; Zhu et al., 2019] revealed thickened crust, high bulk crustal Vp/Vs ratio, and low-velocity zone in the mid-crust beneath the CBS volcano, suggesting a magma reservoir related partial melt in the mid or lower crust beneath the volcano (Figures 6 and 7). However, the spatial distribution of the seismic rays showing S-wave shadows suggests that molten or partially molten magma may exist in the crust or upper mantle or at both depths.

Recently, a two-layer magma chamber/reservoir model has been proposed for the CBS volcano: one chamber is located in the crust, and the other is in the upper mantle [e.g., Fan et al., 2007; Kim et al., 2017; Chen et al., 2021; Liu et al., 2021]. Using the transdimensional Bayesian inversion of ambient noise data for the CBS, Kim et al. [2017] suggested a two-layer magmatic system consisting of a shallow felsic body overlying mafic underplating. The two-layer magma chamber model was further supported by the mineralogical, petrological, geochemical, isotopic, and full-waveform seismic tomographic evidence presented in the recent study of Chen et al. [2021]. This study determined that the two-layer magma chamber is mainly concentrated at depths of -10km and 40-60km (Figure 35). Liu et al. [2021] proposed a “double chambers” model showing the migration of magma from the deep source to a shallow reservoir of CBS volcano in response to dynamic stress perturbations caused by the 2002 Wangqing deep-focus earthquake in the stagnant Pacific Plate beneath NE Asia, which could trigger the 2002–2005 unrest of CBS

volcano. In Liu et al. [2021] model, an upwelling plume derived from the mantle transition zone (410km) could accumulate in the upper mantle transition zone. Injection of deep-sourced magma into the shallow magma chamber led to anomalous magma stirring and degassing, which pressurized the shallow magma chamber and facilitated intrusion of gas-enriched magma through cracks above the magma body. Hydrothermal fluid migration was influenced by the crack intrusion of magmas. Although the mechanism of the double-layer magma chamber model and the exact depth of the magma chamber are debated, the mantle chamber continually supplies trachybasalt influx from below to the crustal chamber, making the CBS volcano a long-life active volcano.

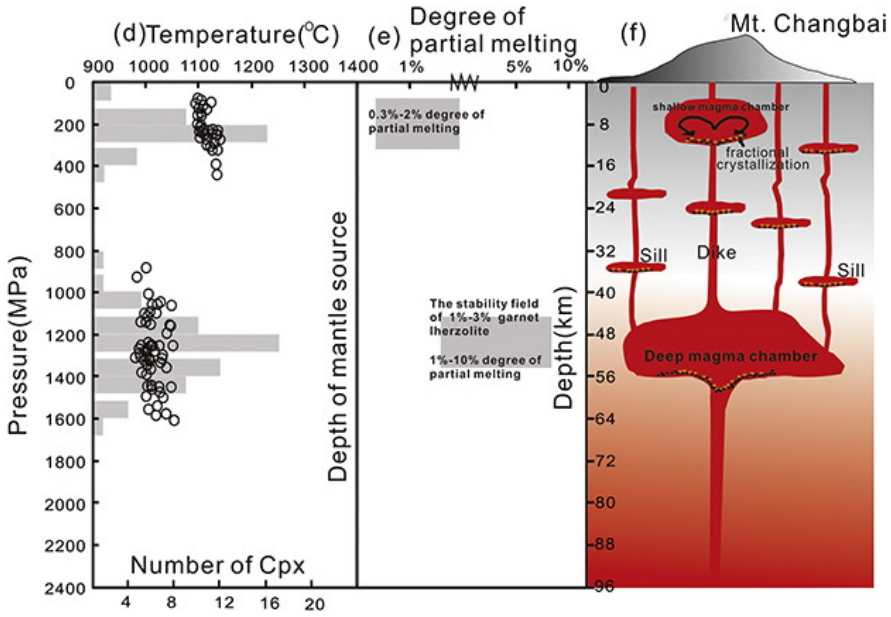


**Figure 35**. Two-layer magma chamber model beneath the CBS volcano. The temperature and degree of partial melting for the two chambers are also shown. This figure is taken from Figure 14 in Chen et al. [2021].

The double-layer magma chamber models proposed by different researchers can explain the S-wave shadows observed in our study. In those double-layer magma chamber models, the chamber/reservoir in the upper mantle is larger than that in the curst and thus dominates the observed S-wave shadows. Future studies of the crust in regions far from volcanos but showing significant S-wave shadows are needed. For example, we observed significant S-wave shadows at many stations in the northwest of NE China (Figures 20 and 21). The receiver functions and surface waves analysis on those stations will help to detect anomalies such as thickened crust, high crustal bulk Vp/Vs ratio, and low-velocity zones. If we rule out crustal anomalies beneath those stations, we can confirm that their S-wave shadows originate from molten magma in the upper mantle.

The CRT program is a powerful tool for dynamic ray tracing simulations. In this study, we performed extensive ray tracing calculations using a layered model and determined the spatial positions and travel times of rays with S-wave shadows and P-wave delays. Future ray tracing simulations will focus on 3D models and the dynamic properties of seismic rays. To set up a 3D model representing a low-velocity zone or magma reservoir, we will collect all seismic rays showing S-wave shadows and P-wave delays and compare the overlapped areas of these seismic rays to the tomographic models. We will finally characterize the magma reservoir beneath the CBS by adjusting the 3D models until the ray tracing results console the observed S-wave shadows and P-wave delays.

# 7 CONCLUSIONS

In this study, we judiciously selected 97 deep-focus earthquakes that occurred within the Wadati-Benioff seismic zone along with the subducting Pacific slab beneath the Japan Sea and the northeastern Eurasian continent margin. We collected seismograms of these events recorded by 5 temporal seismic networks (1U, XI, XL, YP, and V0) and 3 permanent seismic networks (HL, JL, and LN) deployed in NE China. In processing and analyzing these seismograms, we observed significant S-wave shadows and P-wave delays associated with the magma reservoir of the CBS volcano, providing direct evidence for the presence of molten or partially molten magma. The seismic ray tracing simulations for these deep-focus earthquakes show that the spatial distribution of seismic rays with S-wave shadows differs from that of the seismic rays with P-wave delays. The seismic rays with P-wave delays expand over larger areas than those with S-wave shadows. The seismic rays with P-wave delays are generally confined to large-scaled low-velocity zones consistent with the previous tomographic models. The low-velocity zones may contain molten or partially molten cores representing magma reservoirs responsible for the S-wave shadows observed on the surface. It is possible that molten or partially molten magma reservoirs exist in the crust or upper mantle or at both depths.

# 8 REFERENCES

Červeny, V. and Klimeš, L. (1984). Synthetic body wave seismograms for three-dimensional laterally varying media, *Geophys. J. R. astr. Soc*., 79, 119 – 133.

Červeny, V., Klimeš, L. and Psencik, I. (1988). Complete seismic ray tracing in three-dimensional structures, In: D. Doornbos (Editor), *Seismological Algorithms—Computational Methods and Computer Programs*, Academic Press, San Diego, 469.

Chen, H.-W. (1998). Three-dimensional geometrical ray theory and modelling of transmitted seismic energy of data from the Nevada Test Site, *Geophys. J. Int*., 133, 363 – 378.

Chen, Y. and F. Niu (2016). Joint inversion of receiver functions and surface waves with enhanced Preconditioning on densely distributed CNDSN stations: Crustal and upper mantle structure beneath China, *J. Geophys. Res*. *Solid Earth*, 121, doi:10.1002/2015JB012450.

Chen, S.-S. S.-G. Lee, S. Simute, A. Fichtner, T. J. Lee, Y.-S. Lee, J.-Q. Liu and R. Gao (2021). Geochemical and seismic tomography constraints of two-layer magma chambers beneath the bimodal volcanism: A case study of late Cenozoic volcanic rocks form Ulleung Islang and Mt. Changbai (Paektu), Chemical Geology, 581, doi.org/10/1016/j.chemgeo.2021.120386.

Duan, Y.-H., Zhang, X.-K., Liu, Z., Yuan, Q.-X., Xu, Z.-F., Wang, F.-Y., Fang, S.-M. and Yang, Z.-X. (2005). Study on crustal structures of Changbaishan-Jingpohu volcanic area using receiver functions, *C. J. Geophys*., 48, 389 – 396.

Fan, Q. C., Sui, J.L., Wang, T.H., Li, N., Sui, Q. (2007). History of volcanic activity, magma evolution and eruptive mechanisms of the Changbai volcanic province, *Geol. J. China Univ*. 13, 175–190 (in Chinese with English abstract).

Hammond, J. O. S., Wu, J.-P., Ri, K.-S., Wei, W., Yu, J.-N., and Oppenheimer, C. (2020). Distribution of partial melts beneath Changbaishan/Paektu volcano, China/Democratic People's Republic of Korea, *Geochemistry, Geophysics, Geosystems*, 21, e2019GC008461, doi:org/10.1029/2019GC008461.

Hetland, E., Wu, F., and Song, J. (2004). Crustal structure in the Changbaishan volcanic area, China, determined by modeling receiver functions, *Tectonophysics*, 386, 157-175.

Huang, J. and Zhao, D. (2006). High-resolution mantle tomography of China and surrounding regions, *J. Geophys. Res.*, 111, B09305, doi:10.1029/2005JB004066.

Kang, T., Baag, C. and Chu, K. (2011). Volcanic eruptions and seismicity of Mt. Baekdu (Changbai) occurred in the historical time, *American Geophysical Union, Fall Meeting 2011*, Abstract ID: S51E-07.

Kennett B. L. N., Engdahl E. R. and Buland R. (1995). Constraints on seismic velocities in the earth from travel times, *Geophys. J. Int.*, 122, 108-124.

Kim, S., Tkalčić, H., & Rhie, J. (2017). Seismic constraints on magma evolution beneath Mount Baekdu (Changbai) volcano from transdimensional Bayesian inversion of ambient noise data. Journal of Geophysical Research: Solid Earth, 122, 5452–5473. https://doi.org/10.1002/2017JB014105.

Lei, J. and D. Zhao (2005). P-wave tomography and origin of the Changbai intraplate volcano in Northeast Asia, *Tectonophysics*, 397, 281– 295.

Li, Y., Wu, Q. Pan, J., and Sun, L. (2012). S-wave velocity structure of northeastern China from joint inversion of Rayleigh wave phase and group velocities, *Geophys. J. Int.*, 190, 105-115, doi:10.1111/j.1365-246X.2012.05503.x.

Lin, C.-H. (2016), evidence for a magma reservoir beneath the Taipei metropolis of Taiwan from both S-wave shadows and P-wave delays, *Scientific Reports*, 6, 39500.

Lin, C.-H., Y.-C. Lai, M.-H. Shih and H.-C. Pu (2018). Seismic anatomy of molten sill reservoirs by both S-wave shadows and reflections, *Scientific Reports*, 8, 16401.

Liu, Z., Zhang, X.-K., Wang, F.-Y., Duan, Y.-H., & Lai, X.-l. (2005). 2-D crustal Poisson's ratio from seismic travel time inversion in Changbaishan Tianchi volcanic region, *Acta Seismologica Sinica*, 18(3), 345–353.

Liu G, Li C, Peng Z, Liu Y, Zhang Y, Liu D, Zhang M and Pan B (2021). The 2002–2005 Changbaishan Volcanic Unrest Triggered by the 2002 M 7.2 Wangqing Deep Focus Earthquake, *Front. Earth Sci.* 8:599329, doi: 10.3389/feart.2020.599329.

Qiu, G. G., Pei, F. G., Fang, H., Fang, H., Du, B. R., Zhang, X. B., et al. (2014). Analysis of magma chamber at the Tianchi volcano area in Changbai mountain, *Chinese J. Geophys.*, 57(10), 3466–3477. (in Chinese).

Ri, K.-S., Hammond, J. O. S., Ko, C.-N., Hyok, K., Yun, Y.-G., Pak, G.-J., Ri, C.-S., Oppenheimer, C., Liu, K. W., Lacovino, K., and Ryu, K.-R. (2016). Evidence for partial melt in the crust beneath Mt. Paektu (Changbaishan), Democratic People's Republic of Korea and China, *Sci. Adv.*, doi:10.1126/sciadv.1501513.

Song, J., Hetland, E. A.,Wu, F. T., Zhang, X., Liu, G., & Yang, Z. (2007). P-wave velocity structure under the Changbaishan volcanic region, NE China, from wide-angle reflection and refraction data. *Tectonophysics*, 433(1-4), 127–139.

Sun, W.-B. and He, Y.-S. (2004). The feature of seismicity in Northeast China and its relation to the subduction of the Japan sea plate, *Earthquake and Geology*, 26(1), 122 – 132.

Tang, J., Deng, Q. and Zhao, G. (2001). Electric conductivity and magma chamber at the Tianchi volcano area in Changbaishan, *Seismol. Geol.*, 23, 191–200 (in Chinese).

Tang, Y., M. Obayashi, F. Niu, S. P. Grand, Y. J. Chen, H. Kawakatsu, S. Tanaka, J. Ning and J. F. Ni (2014). Changbaishan volcanism in northeast China linked to subduction-induced mantle upwelling, Nature Geoscience, 2014, doi:10.1038/ngeo2166.

Tao, K. Liu, F. Ning, J. Chen, Y. Grand, S. Kawakatsu, H., Tanaka, S. Obayashi, M., and Ni, J. (2014). Crustal structure beneath NE China imaged by NECESSArray receiver function data, *Earth Planet. Sci. Lett.*, 398, 48-57, doi:10.1016/j.epsl.2014.04.043.

Wei, H., G. Liu and J. Gill (2013). Review of eruptive activity at Tianchi volcano, Changbaishan, northeast China: Implications for possible future eruptions, *Bull. Volcanol.*, 75, 706.

Wu, J., Jiao, W., Ming, Y., & Su, W. (2006). Attenuation of coda waves at the Changbaishan Tianchi volcanic area in Northeast China. *Pure and Applied Geophysics*, 163(7), 1351–1368.

Wu, J., Ming, Y., Fang, L., & Wang, W. (2009). S-wave velocity structure beneath Changbaishan volcano inferred from receiver function. *Earthquake Science*, 22, 409–416.

Xu, J., G. Liu, J. Wu, Y. Ming, Q. Wang, D. Cui, Z. Shangguan, B. Pan, X. Lin, and J. Liu (2012). Recent unrest of Changbaishan volcano, northeast China: A precursor of a future eruption? *Geophys. Res. Lett*., 39, L16305, doi:10.1029/2012GL052600.

Yang, Y., Lei, J., Ai, Y., Zhang, G., Sun, C., Fan, E., et al. (2019). Crustal structure beneath Northeast China from ambient noise tomography. *Physics of the Earth and Planetary Interiors*, 293, 106257.

Zhang, C., Zhang, X., Zhao, J., Liu, B., Zhang, J., Yang, Z., Hai, Y., Sun, G. (2002). Crust-mantle structure of the Changbaishan Tianchi volcanic region and its vicinity: An exploratory study and inferences, *Chinese J. Geophys.*, 45, 862-871.

Zhao, D. and Tian, Y. (2013). Changbai intraplate volcanism and deep earthquakes in east Asia: a possible link? *Geophys. J. Int.*, 195, 706-724, doi:10.1093/gji/ggt289.

Zhu, G. Shi, Y. and Tackley, P. (2010). Subduction of the western Pacific plate underneath Northeast China: Implications of numerical studies, *Phys. Earth Planet. Int*., 178, 92-99, doi:10.1016/j.pepi.2009.10.008.

Zhu, H., Tian, Y., Zhao, D., Li, H., & Liu, C. (2019). Seismic structure of the Changbai intraplate volcano in NE China from joint inversion of ambient noise and receiver functions. *J. Geophys. Res.: Solid Earth*, 124, 4984–5002. https://doi.org/10.1029/2018JB016600.